

AD-A099 720

JAYCOR ALEXANDRIA VA
MODELING OF IMPIOLED ANNULAR PLASMAS. (U)
MAY 81 R E TERRY, J U GUILLORY
JAYCOR-J207-81-004

F/6 20/9

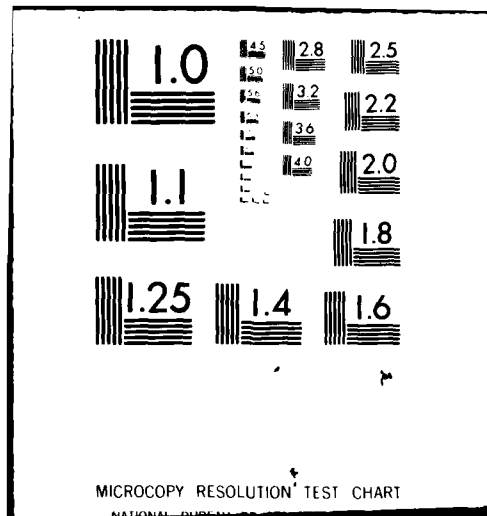
DNA001-79-C-0189

UNCLASSIFIED

NL

$$\frac{1}{\sqrt{\pi}} \int_{-\infty}^{\infty} e^{-x^2} dx = 1$$

END
DATE
FILMED
6-8
DTIC



LEVEL ⁽¹⁾

AD A099720

JAYCOR

DTIC
ELECTE
JUN 4 1981
S A D

This document has been approved
for public release and sale; its
distribution is unlimited.

DTIC FILE COPY

81 6 04 057

205 South Whiting Street
Alexandria, Virginia 22304

9) ANNUAL REPORT ON
MODELING OF IMPLoded
ANNULAR PLASMAS

13) Contract DNA-001-79-C-0189

10) Robert E. Terry
John U. Guillory

14) JAYCOR REPORT NO.
JAYCOR-J207-81-004

11 May 1981

Submitted to:

Defense Nuclear Agency
Washington, D.C.

This report has been approved
for public release and sale; its
distribution is unlimited.

DTIC
SELECTED
JUN 4 1981

A

393453

CONTENTS

	<u>Page</u>
I. INTRODUCTION AND EXECUTIVE SUMMARY.	1
II. SYSTEMATIC YIELD TRENDS RESULTING FROM THE PRESENT CORE-CORONA MODEL	5
A. Code Improvements over this Contract Period	5
B. The Standard Yield Experiment	10
C. Dynamics of Typical Implosions.	13
D. Standard Yield Experiment Parameter Studies	17
E. Testing the Yield Dependence on a Possible Scaling Parameter	24
III. ELECTRODYNAMIC MODELS OF ANNULAR PLASMA-LOADED DIODES BASED ON A GENERALIZED HERTZ VECTOR POTENTIAL	26
A. Introduction.	26
B. The Fundamentals Revisited.	27
C. Simple Solutions in the Steady-State Plane-Parallel Waveguide.	31
D. Explicit Source Transformations of the Wave Equation and the Separation of Time Scales.	34
E. The 1-D Electromagnetohydrodynamics (EMHD) Model for the Plane Parallel Waveguide.	35
IV. IMPLICATIONS OF DISCHARGE BEADING WITH LOW-DENSITY INTERCONNECTION REGIONS	38
Introduction.	38
Current	39
Voltage Drop in Low Density Regions	40
Joule Heating	42
Cooling Rates Offsetting Joule Heating.	43

	<u>Page</u>
Power Delivery.	46
Peak Electron Temperature	47
Inductive Effects	49
Justification of Drift-Speed-Limited Current.	51
Application to Cylindrical Implosions and the SPLAT Code.	53
Sausage Instability Dynamics.	55
V. CURRENT PROBLEMS	57
A. Improved Numerical Methods.	57
B. Alternate Thermodynamic Variables for Ionization Dynamics	58
REFERENCES	59
APPENDIX A - Field Representations	A1
APPENDIX B - Hertz Vector Potential for the Plasma Loaded Waveguide.	B1
APPENDIX C - Coupling of Fluid and Field Equations	C1
APPENDIX D - Wave Equation Quadratures	D1

Accession For	
NTIS GRA&I	<input checked="" type="checkbox"/>
DTIC TAB	<input type="checkbox"/>
Unannounced	<input type="checkbox"/>
Justification	
<i>file on file</i>	
By	
Distribution/	
Availability Codes	
Dist	Avail and/or Special
A	

CHAPTER I. INTRODUCTION AND EXECUTIVE SUMMARY

During 1980, JAYCOR has continued its modeling of the implosion dynamics and radiative output of diode-imploded annular plasmas, in close coordination with work ongoing at the Naval Research Laboratory.

→ This report treats three areas of advance during the 1980 effort: (I) improvements to the 1-D strongly-coupled plasma implosion and radiation code SPLAT and results of radiative yield studies using the code; (II) development of formalism for solving the field penetration/skin-depth problem in an inhomogeneous, time-varying imploding conductor in a plasma-loaded diode; (III) circuit equation and scaling of hard radiation in the presence of fully developed sausage instability (beading) of the assembled plasma. In addition, a short section (Chapter V) is devoted to work in progress: high-accuracy matrix inversion techniques and interpolators for solving the generalized Hertz vector equations used in II above, and for following CRE equations and diffusive behavior in general; and, beginning plans for modifying 1-D MHD codes, making them compatible with the field-diffusion and corona programs and with CRE radiation packages. ←

I. The code improvements to SPLAT are:

- (A) a rudimentary two-bin spectral resolution of the radiative output (formerly only total radiated energy was shown). This still leaves continuum radiation separate, however, and in neither spectral bin.
- (B) scaling laws (Eqn's. 1 abc, 2ab) for density and electron temperature-dependence of the low-energy and high-energy radiative yields $Y^<$ and $Y^>$;
- (C) separate opacity/escape treatments for the three spectral categories;

- (D) more realistic exchange of energy between flow kinetic energy and thermal, during and just after the "collection" or mixing process;
- (E) energy-conserving averaging of T_e and T_i when these two attempt to develop large rapid oscillation; and finally
- (F) incorporation of a CRE radiation package for Argon.

Yield studies for Aluminum radiation vs wire array mass, initial radius, and current penetration radius have been done, and these complement earlier studies of the variation with peak voltage and generator risetime. The total yield is optimized at a certain mass, although $Y^>$ optimizes generally at a considerably lower mass, as physically expected since large masses cannot be heated to the required temperatures. Peak T_e of course decreases with increasing load mass, while the peak density-squared increases, until the mass is too large to be imploded in the required time. Other parameters being equal, an optimum initial radius is seen for both Y^{TOT} and $Y^>$; larger initial radii have lower peak temperatures because the assembly occurs after the current has decayed - the plasma coasts in rather than still being strongly squeezed at assembly. Current-crowbarring may weaken or shift this optimum. Smaller-radius loads of the same mass implode too quickly and tend to be cool, opaque and subject to Simple Collapse, with mostly blackbody losses. Intermediate radius loads exhibit well matched, Pause-and-Collapse implosions in which the temperatures are high enough to forestall immediate collapse and the densities are high enough for significant radiation but low enough to allow the radiation escape rate to match that of kinetic energy to thermal conversion.

The dynamics of the radiation pulse mirrors the temperature-dependence of the radiation output curve, its multiple peaks representing qualitatively a time history of T_e . A single peak is characteristic of low

temperatures, ascending and descending the low-temperature side of the L-shell peak. Double-peaked or triple-peaked radiation pulses tend to be correlated with higher K-shell yields, although in real plasmas thermal gradients, i.e., $T_e(r)$, may tend to diffuse and merge the individual peaks. (SPLAT is isothermal in the core plasma.)

II. The electric and magnetic field penetration into the imploding, time-varying plasma influences the thickness of the current-carrying region and the ratio of classical (core) to nonclassical (corona) currents. This affects the circuit relation, heating rates, and the matching of the implosion to the driver. To solve this problem, one considers first the coupled wave-diffusion equations in E and B, and combines them to form a single differential equation in a higher order potential Z, which is a generalization of the Hertz vector in classical electromagnetic cavity theory. The equation for Z, its well-posed boundary conditions, and special techniques for its computational solution, have been developed during this past year's contract effort, and are reported in Section III of this report, with mathematical details largely relegated to appendices A-D. As presently handled in the SPLAT code, magnetic diffusion is frozen in at an arbitrarily chosen value at early time (when the conductivity should be low), because the plasma conductivity rises to exclude further field penetration. SPLAT code results are reasonably sensitive to the current penetration, motivating us to do this feature in a more self-consistent way. But the Hertz potential equation requires sophisticated computer techniques which are being developed under the 1981 funding.

III. Section IV of this report treats beaded discharges and the implications for the hard component of the radiation. It assumes that the fully-developed nonlinear stage of the sausage instability necks the plasma column off in many places to produce relatively low-density regions. The condition for nonclassical conduction in these regions is remarkably lenient at high temperature, so we investigate the consequences of the regions being nonclassical at all radii. At high E-fields, this gives

lower current than with classical conduction, but gives greatly enhanced ohmic heating, to tens of keV, and this energy is deposited in the denser beads, producing hard radiation. Depending on the E-field penetration, which is enhanced by the unstable fluctuations, this effect may produce high power levels of such radiation, and offers the prospect of copious K-shell radiation from plasmas whose mass is too large to allow the temperatures required for thermal K-shell emission. The efficiency is high if much of the voltage drop occurs in the low-density regions between beads, and if these regions are long enough to allow adequate heating before deposition.

A short description of ongoing work is contained in Section V of this report. Two areas are under development: high-order interpolation techniques, which are necessary for computer solution of the magnetic field diffusion problem but also useful in radiation modeling and MHD codes, and the modification of a 1D MHD code to treat the dynamics of low-mass higher-temperature imploding plasmas which are not "strongly-coupled" and thus not properly described by the SPLAT code. (Typical Argon implosions, for example, probably do not have the viscosity necessary for the SPLAT description.) Because of the potential importance of the field diffusion and radiation processes, we are working toward making the MHD code interface easily with the generalized Hertz-potential solver and the local temperature equations with CRE radiation.

CHAPTER II. SYSTEMATIC YIELD TRENDS RESULTING FROM THE PRESENT CORE-CORONA MODEL

A. Code improvements over this contract period

The existing simplified core-corona implosion model¹ has been modified to provide spectral resolution in the radiative yields computed during the course of a single implosion. Extending previous techniques, the radiative emission from an aluminum plasma of fixed density and radius is calculated as a function of electron temperature using the collisional-radiative equilibrium (CRE) model due to Duston and Davis². The size of the cylindrical radiator is set to a small value, e.g. 0.05 cm, and the output radiated energy decomposed into three categories: "L-shell" or $h\nu < 1$ keV, "K-shell" or $h\nu > 1$ keV, and recombination continuum. One may then derive an equivalent volume emission rate (ϵ) from this single line source and these results are represented by

$$\epsilon^<(n_I^0, T_e) = \exp \left\{ \sum_k b_k^< \left[\ln(T_e / 0.3) \right]^k \right\} \quad (1a)$$

$$\epsilon^>(n_I^0, T_e) = \exp \left\{ \sum_k b_k^> \left[\ln(T_e / 0.7) \right]^k \right\} \quad (1b)$$

$$\epsilon^{FB}(n_I^0, T_e) = \exp \left\{ \sum_k b_k^{FB} \left[\ln(T_e / 0.5) \right]^k \right\} \quad (1c)$$

at the reference density n_I^0 . This emission is then subjected to a density scaling appropriate to each radiation category, in particular, a reasonable approximation³ is obtained using

$$\begin{aligned} \epsilon^{>,FB} &\sim (n_I/10^{18})^{1.5} & n_I > 10^{18} \\ &(n_I/10^{18})^2 & n_I < 10^{18} \end{aligned} \quad (2a)$$

$$\begin{aligned} \epsilon^< &\sim (n_I/10^{16})^{1.5} & n_I > 10^{16} \\ &\sim (n_I/10^{16})^2 & n_I < 10^{16} \end{aligned} \quad (2b)$$

Plots of the spectral representations $\epsilon^<$, $\epsilon^>$, ϵ^{FB} are shown in Figure 1 as $P^<$, $P^>$, P^{FB} respectively arising from a CRE calculation with $n_I^0 = 1.0 \cdot 10^{19} \text{ cm}^{-3}$ and a radius of 0.05 cm. The curve P_{rad} is the sum of the individual representations $P^<$, $P^>$, P^{FB} and can be seen to reproduce the original CRE results (marked by a " \square ") to within 5 % or better over the temperature domain of interest here. The equivalent volume emission rate from a black body of the same size ($\sigma T_e^4 / \pi r_0^2$) is plotted for comparison.

Using this $\epsilon(n_I, T_e)$ as a source term, the net radiative loss from any plasma density profile $[n_I(r_i, t) \text{ and } T_1(t)]$ generated by the core-corona model can be developed once the proper opacity corrections are calculated in a local approximation. At selected locations r_i within the density profile $\epsilon^<(n_I(r_i), T_1)$, $\epsilon^>(n_I(r_i), T_1)$, $\epsilon^{FB}(n_I(r_i), T_1)$ and $\epsilon^{FF}(n_I(r_i), T_1)$ (Bremsstrahlung) are calculated and subjected to an additional attenuation based on the probability of escape (P_e) from the specified location r_i . The P_e depends upon the optical depth τ_i and an accurate approximation to this escape probability is to compute optical depths along each of two paths, inclined to the radius vector along a chord representing the mean angle of emission for a cylindrically symmetric radiator, and average the P_e over the two path lengths. This implies that an effective optical depth can be assigned to r_i once the line integral

$$\bar{\ell}_i \equiv \int_{r_i}^a d\ell \frac{n_I(\ell)}{n_I(r_i)}$$

is computed over the short(S) and long(L) path to the plasma surface. Each point r_i is thus assigned two optical depths for each spectral category, e.g. $\tau_{i,S}^<$ and $\tau_{i,L}^<$, with these optical depths computed from $\bar{\ell}_{i,S}$, $\bar{\ell}_{i,L}$. The appropriate scattering cross-sections for a 0.5 keV "L-shell" line, a 1.5 keV "K-shell" line, Al photo-ionization/recombination, and Bremsstrahlung provide $\tau_{S,L}^<(r_i)$, $\tau_{S,L}^>(r_i)$, $\tau_{S,L}^{FB}(r_i)$ and $\tau_{S,L}^{FF}(r_i)$ respectively once $\bar{\ell}_{i,S}$ and $\bar{\ell}_{i,L}$ are known.

The final radiative loss from each point in the density profile can be written

P_{rad} (erg/cm³ sec) as a function of T_e (keV)

[from a 0.05 cm radius cylindrical Al plasma with $n_i = 1.0 \cdot 10^{19}$ cm⁻³]

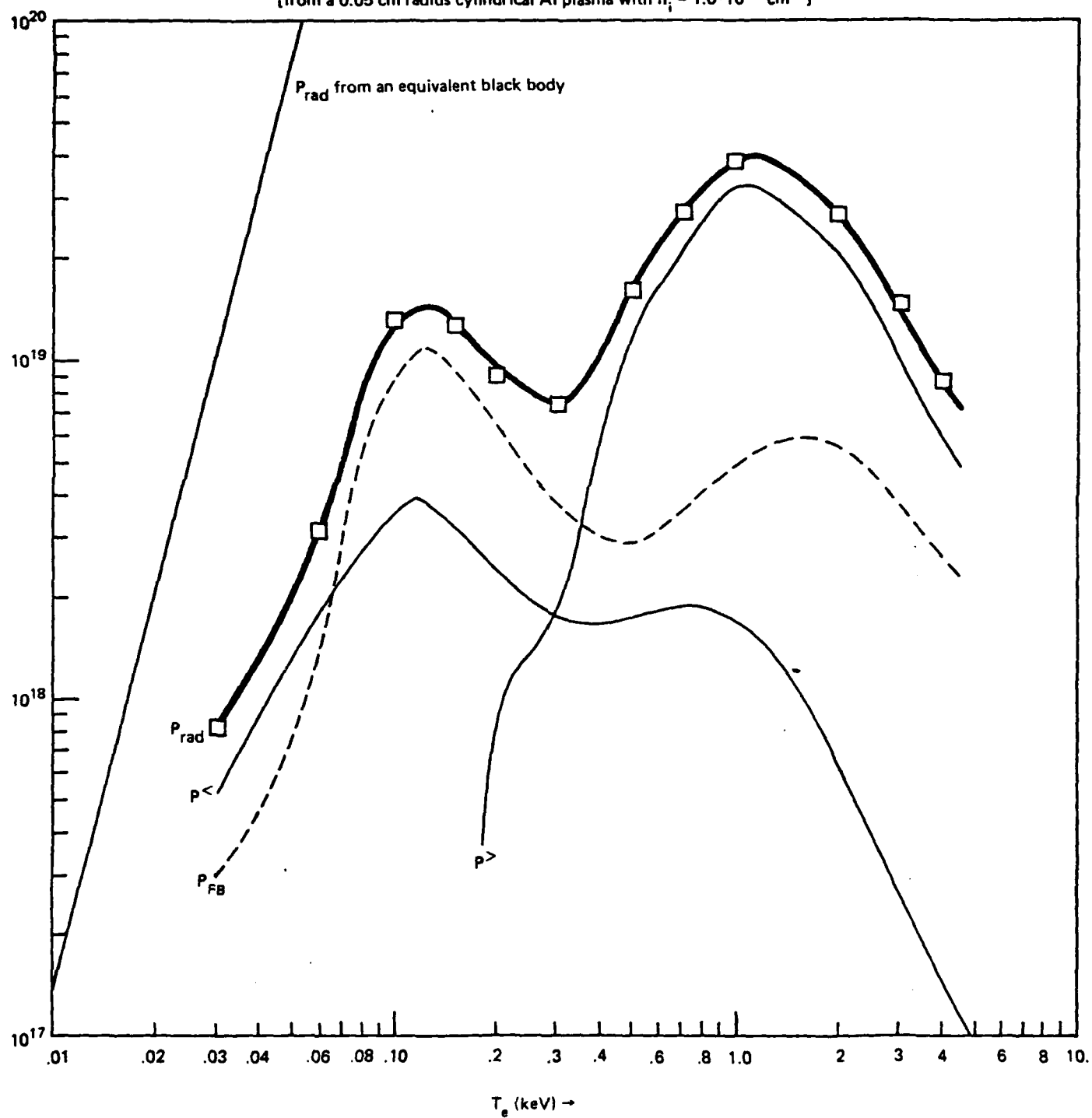


Figure 1

$$\epsilon_T(n_I(r_i), T_i) = \epsilon^{FF} \cdot \frac{1}{2} (e^{-\tau_S^{FF}} + e^{-\tau_L^{FF}}) + \epsilon^{FB} \cdot \frac{1}{2} (P_e(\tau_S^{FB}) + P_e(\tau_L^{FB}))$$

(3)

$$+ \epsilon^> \cdot \frac{1}{2} (P_e(\tau_S^>) + P_e(\tau_L^>)) + \epsilon^< \cdot \frac{1}{2} (P_e(\tau_S^<) + P_e(\tau_L^<))$$

and this function is radially integrated to produce the radiant energy loss at each time step. As a spectral diagnostic, the radially integrated power loss for lines ($P^<$, $P^>$) and continuum ($P^{FF} + P^{FB}$) is reported separately and time integrated as well to provide accumulated yields in the three categories "L-shell" ($h_\nu < 1$ keV), "K-shell" ($h_\nu > 1$ keV) and all continuum (FF + FB).

Within this local approximation the model plasma is represented (radiatively) as a superposition of uncoupled CRE line sources attenuated by the local probability of escape appropriate to each spectral category. This $P_e(r_i)$ is calculated self-consistently with respect to the density and temperature profile generated by the MHD plasma evolution, and the individual line source strength $\epsilon(n_I, T_i)$ is assigned self-consistently with respect to this evolution. In this context the local radiation approximation is in keeping with the strongly coupled fluid limit used within the core-corona model (at the outset of this research) to simplify the MHD plasma evolution. In a local-radiation limit one has the assumption that the radiative diffusion of energy is so rapid that all the superposed CRE sources are in equilibrium with each other so that there is no need to couple them and iterate in order to establish the excited state populations (note that $n_I(r, t)$ must be a conserved quantity in that iteration). In fact, for optically thick, highly collisional systems it is this very rapid radiative diffusion which helps support the isothermal plasma temperature profile. In short, the thicker the plasma the more appropriate this local radiation limit becomes, and the method can be extended to an arbitrary number of spectral categories.

A similar development has been carried through for Ar and the SPLAT code is now equipped with a radiation package which models either Al or Ar depending on the input choices. The equivalent CRE source profile for Ar is shown in Figure 2.

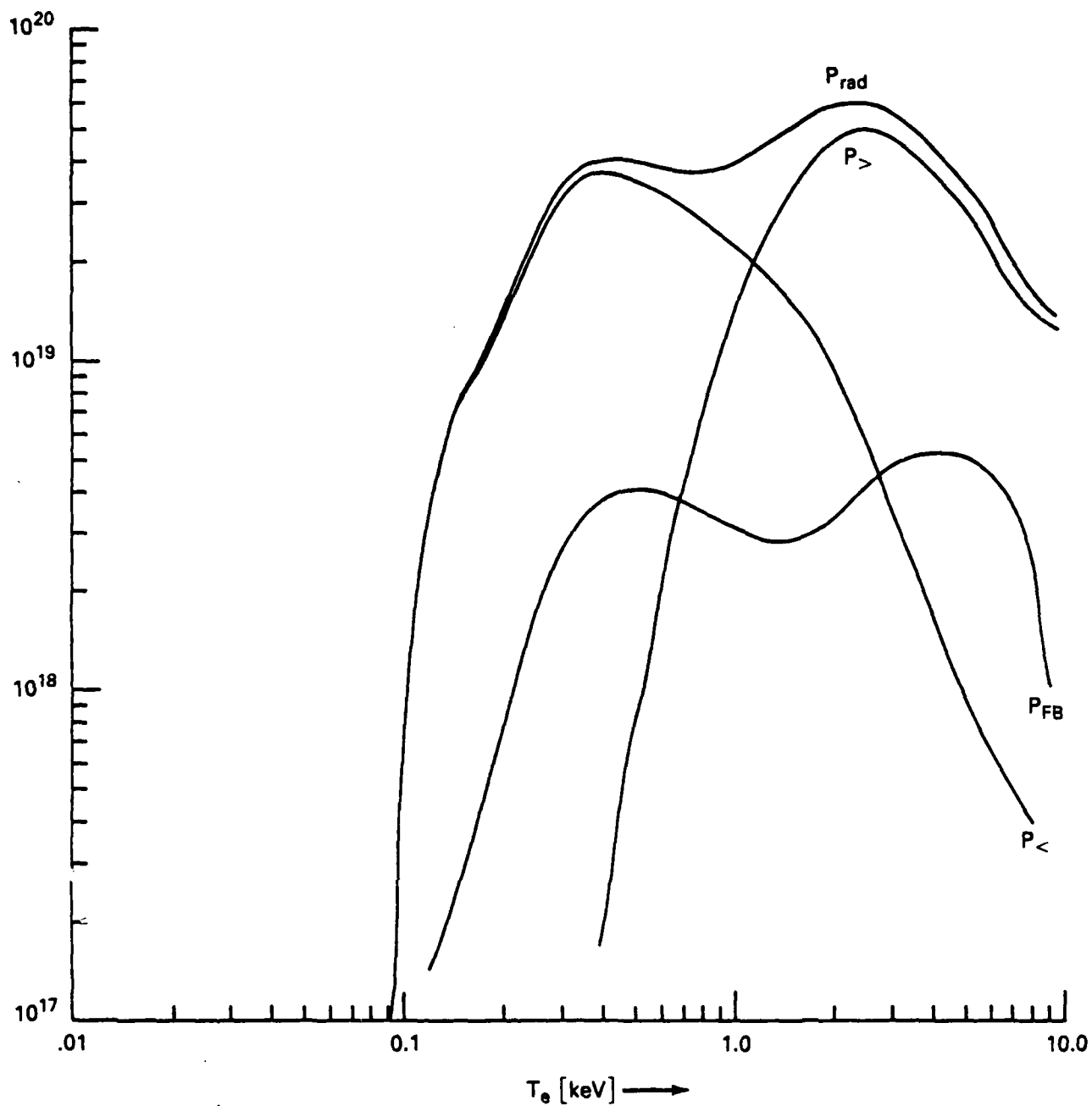


Figure 2. P_{rad} ($\text{erg/cm}^3 \text{ sec}$) as a Function of T_e (keV)
from a 0.001 cm Ar plasma with $n_I = 1.0 \cdot 10^{19} \text{ cm}^{-3}$

A second area of improvement is in the thermalization of the kinetic energy in the flow field ($\frac{1}{2}m_i m_i V_r^2$) during the collection process.⁵ The present technique involves an explicit calculation of the energy residing in this flow at each time step during collection and, when the flow energy at the new time step is less than that at the old, the energy difference is thermalized either by setting a heating rate $\Delta E/\Delta t$ or by instantaneously boosting the core internal energy by ΔE . In addition, energy deficits at the end of the collection process are thermalized over a time scale $\Delta t = (a - r_m)/(c_i - \dot{a})$ characteristic of a shock transit. This models the final momentum propagation to the outer regions of the plasma, as required to bring the velocity profile into a centrally stagnant form when the deceleration of the annulus proceeds from the center outward.

A final improvement is the installation of an internal energy conserving average for T_e and T_i in the core when the energy exchange time τ_{ei} is very short and one seeks to stabilize temperature oscillations. The quantity $u = T_i + Z(T_e)T_e$ is now kept fixed whenever rapid exchange oscillations imply the need to average T_e and T_i . The (usually slow but sometimes significant) electron-ion heat exchanges are now also included in the coronal temperature calculation ($Z\dot{T}_2$).

B. The Standard Yield Experiment

In order to mimic a real experiment with our present core-corona model several constraints must be kept in mind. First, there is every reason to believe that present experiments are most surely not cylindrical in their implosion. The wire/puff gas plasmas tend to close on the axis like a zipper due to inhomogeneities in the electromagnetic fields within the diode cavity. Since no axial variations are followed in the present code, one finds that accurate models of machine driving pulses provide an excess of energy to the 1-D system and assemble it violently on axis. Under some conditions this results in many bounces of the model plasma, which are unrealistic, and the yield figure extracted from the model must take this into account. Second, the present model does not treat the late time behavior of the discharge when "sausage" and "kink" instabilities

are often apparently present. Since the sausage mode, in particular, probably has a significant impact on the (time dependent) discharge impedance and thus on its radial confinement and compression, the yield figure extracted from the present code must avoid the post-implosion phase. Third, the present model does not attempt to treat the "crowbar" effect active in many existing diodes, which keeps the current peaked at a large value while the trapped magnetic energy decays. In a device that does not short out, one expects the current to decay smoothly as the machine's driving voltage decays and this behavior is indeed obtained from our circuit equation. The weakening of the current allows the present model plasma to expand more easily than one might expect in the real experiment and again renders the yield figure developed over the later phases of the implosion inapplicable to existing experiments.

A simple yield observation can be defined that avoids these caveats if one simply presumes that some time window dependent on the bulk plasma motion can be extracted experimentally. For purposes of a general comparison let Y_E be defined as that yield (in any spectral category) developed through a single compression and subsequent expansion of the load, i.e.

$$Y_E \equiv \int_0^{t_E} dt \, P_{\text{rad}}(t_1) \quad (5)$$

with t_E the (expansion) time when the radially outward flow velocity first falls to zero after the initial compression. This choice of a yield measurement removes all late time behavior and represents a realizable measurement once the experimental radiative output is correlated in time with some measure of the plasma flow velocity. The present model can thus be used to study $Y_E^>$, $Y_E^<$, $Y_E^{\text{FF+FB}}$ as functions of some 20 independent model input parameters.

Our recent work focuses on only two of these input parameters, but ones which are clearly related to easily adjusted experimental initial conditions. These are the total mass of the load (M_0) and the location of the density maximum (r_m^0), upon transition to a plasma state, and are easily varied as parameters of the initially self-similar plasma model. These are experimentally equivalent to the number of wires (of fixed diameter) in a load array and the initial radial location of the load array. In order to complete the specification of these studies, a list of the other relevant input parameter ranges is shown in Table I.

Table I. Fixed Initial Parameters

Diode Inductance, L_D	13.5 nh
Generator Impedance, Z_g	0.5 Ω
Maximum $V_{oc}(t)$	1.5 \rightarrow 4.5 MV
Time to reach V_{oc}^{max}	150 ns
Initial current penetration parameter* $g \approx 20 \rightarrow 5$ $g \equiv (r_I/a)^2 / 1 - (r_I/a)^2$	
Initial plasma temperature	15 eV
Initial annulus width	~ 0.14 cm
Return current radius	6 cm

*this adjusts the time-average core/corona current partition $\beta(t)$, with larger g values producing smaller β values.

In modeling experiments which vary the r_m^0 and M_0 parameters, the total number of ions should correspond to the mass of a typical load, and masses corresponding to $[6 \rightarrow 24]$ 1.5 mil Al wires 3 cm in length were used. This provides a $(1.125 \rightarrow 4.50) \times 10^{19}$ range in the total ion number for the load or, equivalently, a load mass range of $[168 \rightarrow 673 \mu\text{g} / \text{cm}]$. The initial profiles containing a fixed number of ions are chosen so as to (i) confine the ions within a 0.2 cm (or less) thick annulus, (ii) provide for surface velocities on the order of the sound speed at $T_{i,e}(t_0) \sim 15$ eV, and (iii) assign surface accelerations which are compatible with the pressure gradients and initial $J_Z \times B_0$ stress profiles. Second, the peak density of the profile is chosen to correspond with the initial load radius and has been varied over $[0.3 \rightarrow 2.0]$ (cm), covering popular experimental choices.

A third important parameter in the profile is $r_I (< a)$, the effective skin depth of the plasma. This choice cannot be set easily by experiment but it is a very important parameter in the yield studies. A range in $g \equiv \frac{(r_I/a)^2}{1 - (r_I/a)^2}$ of $[5.0 \rightarrow 20]$ has been examined in recent work. The wide

domain for g is necessary because so little is known as to its proper value.

In summary the available radius and wire/mass combinations are denoted in later figures by

r_m^0 cm	wires (M_o)				
	6	8	12	16	24
2.05	A6	A8	A12	A16	A24
1.58	B6	B8	B12	B16	B24
0.97	C6	C8	C12	C16	C24
0.68	D6	D8	D12	D16	D24
0.30	E6	E8	E12	E16	E24

with V_p and g continuously variable.

C. Dynamics of Typical Implosions

As a general rule the core/corona implosion falls into one of three distinct trajectory types. These are illustrated below in Figures 3, 4, 5 for the case codes and legends shown. The demarcations between the SC/PC/BC trajectories in the experimental domain $[r_m^0, M_o, V_p, g]$ are rather complex as the radius decreases and not yet mapped out. For the larger radii, however, the transition through PC to rather clear BC trajectories is progressive as the load mass is decreased.

The general importance of the corona is also a strong function of radius r_m^0 and g . The smaller values of r_m^0 tend to produce significant current transport in the corona at peak compression for moderate g values. The larger values of r_m^0 tend to allow most of the current to flow in the core most of the time unless the g values are very large (40 - 80). Clearly the details of this dependence are of interest in load design but more initial condition points in r_m^0 must be developed for such a study. The physical origin of the effect is rooted primarily in two things. First, small r_m^0 loads tend to compress more and thus drive g up as the heating due to assembly occurs. Second, the hot dense core tends to release energy into the corona when its surface density gradients are so stiffened. These effects in concert produce a drop in $\beta \equiv I_{core}/I_{total}$.

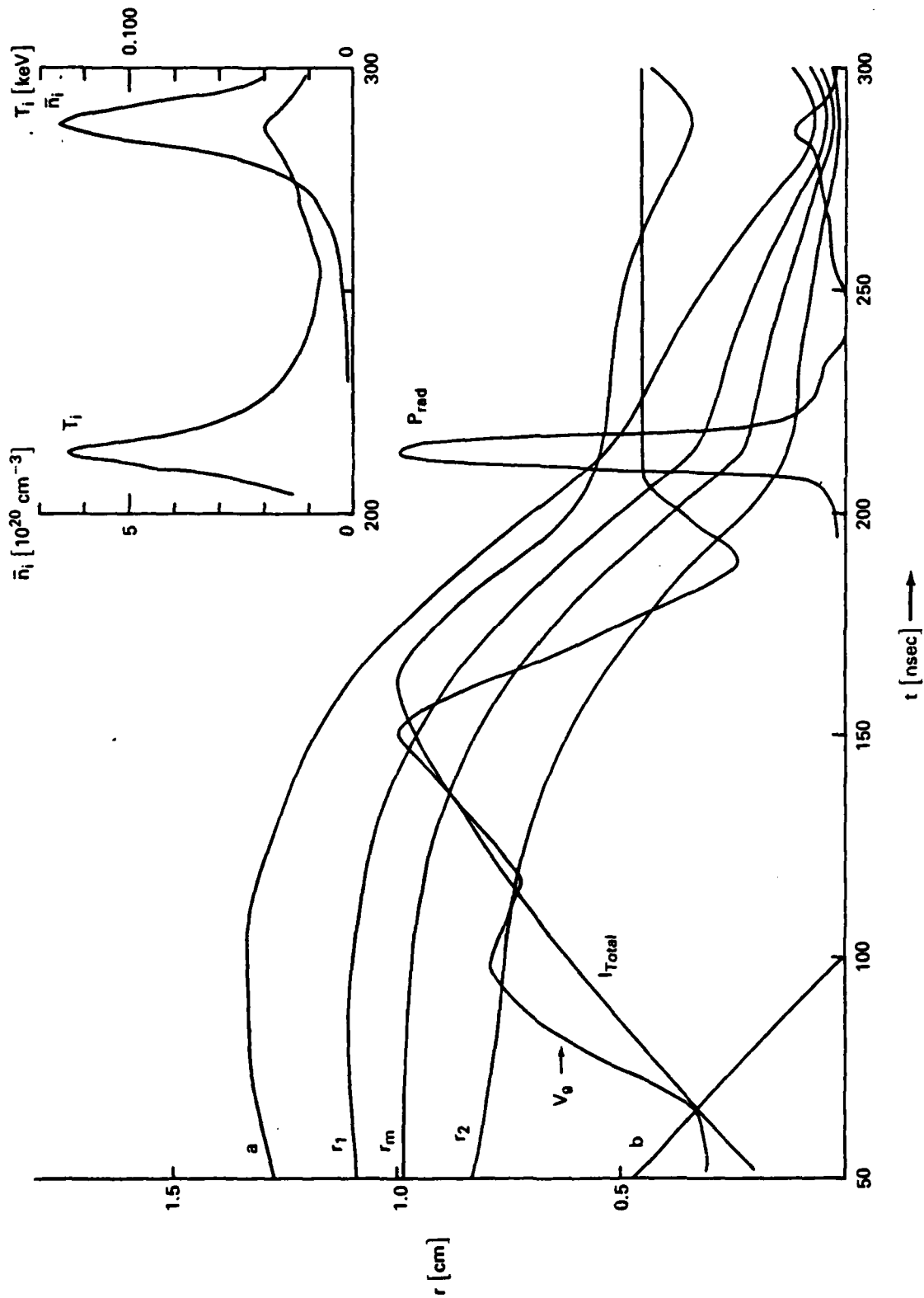


Figure 3. SC Trajectory (Case C12, $g_0 = 3.53$)

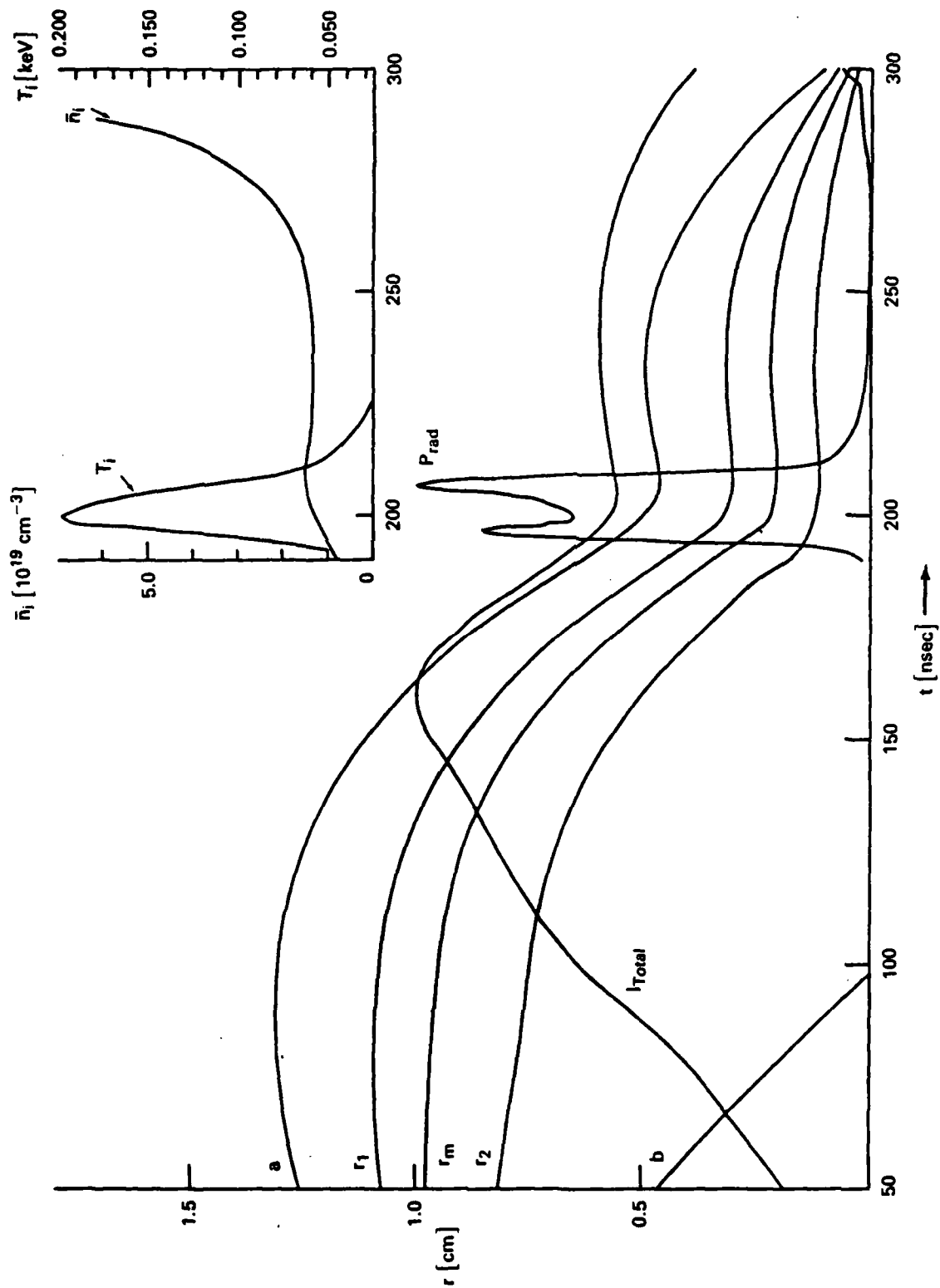


Figure 4. PC Trajectory (Case C16, $g_0 = 7.62$)

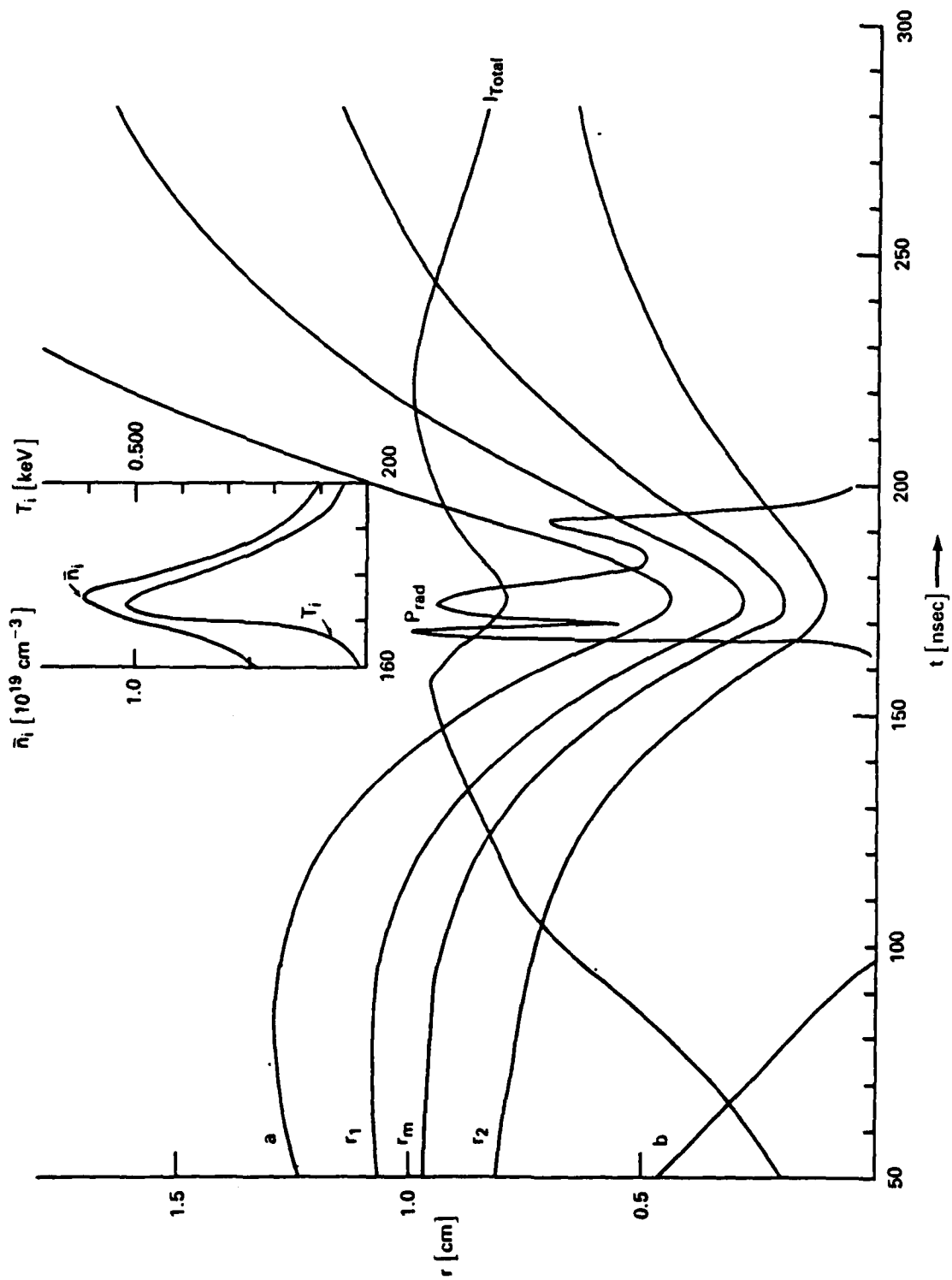


Figure 5. BC Trajectory (Case C12, $g_0 = 13.1$)

At large r_m^0 values the assembly heating generally prevents stiff gradients by holding off the compression. These gradients are available later when the core plasma has been cooled radiatively but then the core has little energy to release into the corona. Hence these effects when separated produce little decay in β .

The radiation pulse-width in these implosions can be seen to vary over a fairly wide range 5-30 nsec. The shorter pulses generally are obtained from cooler, continuum emitting plasmas while some of the larger pulses obtain when the timing of assembly heating, compression and peak current all conspire to produce a hot plasma [600 eV - 1500 eV] that is momentarily confined or quickly recompressed (in a PC sense) by large currents confined at small radius. For the standard voltage rise time mentioned above, only the lower values of r_m^0 (< 1.0) can give rise to this sort of pulse because the load must be able to drift into a nearly assembled state just before the peak voltage and current rise to heat and trap it.

D. Standard Yield Experiment Parameter Studies

Perhaps the easiest variation to examine is the dependence of yield, Y_E in various spectral categories, on the generator peak voltage. In Figure 6, this quantity is plotted for values of $V_p \leq 3.0$ MV using initial case C12 with an assumed $g = 9.0$ for each of three spectral categories: Y_E^{total} , $Y_E^<$, $Y_E^>$. Also shown are the peak temperatures achieved, T_i and the peak compression, \bar{n}_i , over the time frame of the implosion. The generator voltage must be sufficiently large to "ignite" the load, but once this threshold is achieved further voltage increases do not improve the yield significantly. This results from a very much weaker compression for higher voltages (which give higher implosion speeds) as evidenced by a smooth increase in peak temperature and drop in peak density.

A second fundamental variation is that of dependence on the array radius r_m^0 . In Figure 7, the sequence of initial cases E12, D12, C12, B12, A12 has been used to produce the same information as above: Y_E^{total} , $Y_E^<$, $Y_E^>$, T_i , \bar{n}_i , at a fixed voltage $V_0 \approx 1.5$ MV and $g = 9.0$. Here there is a clear

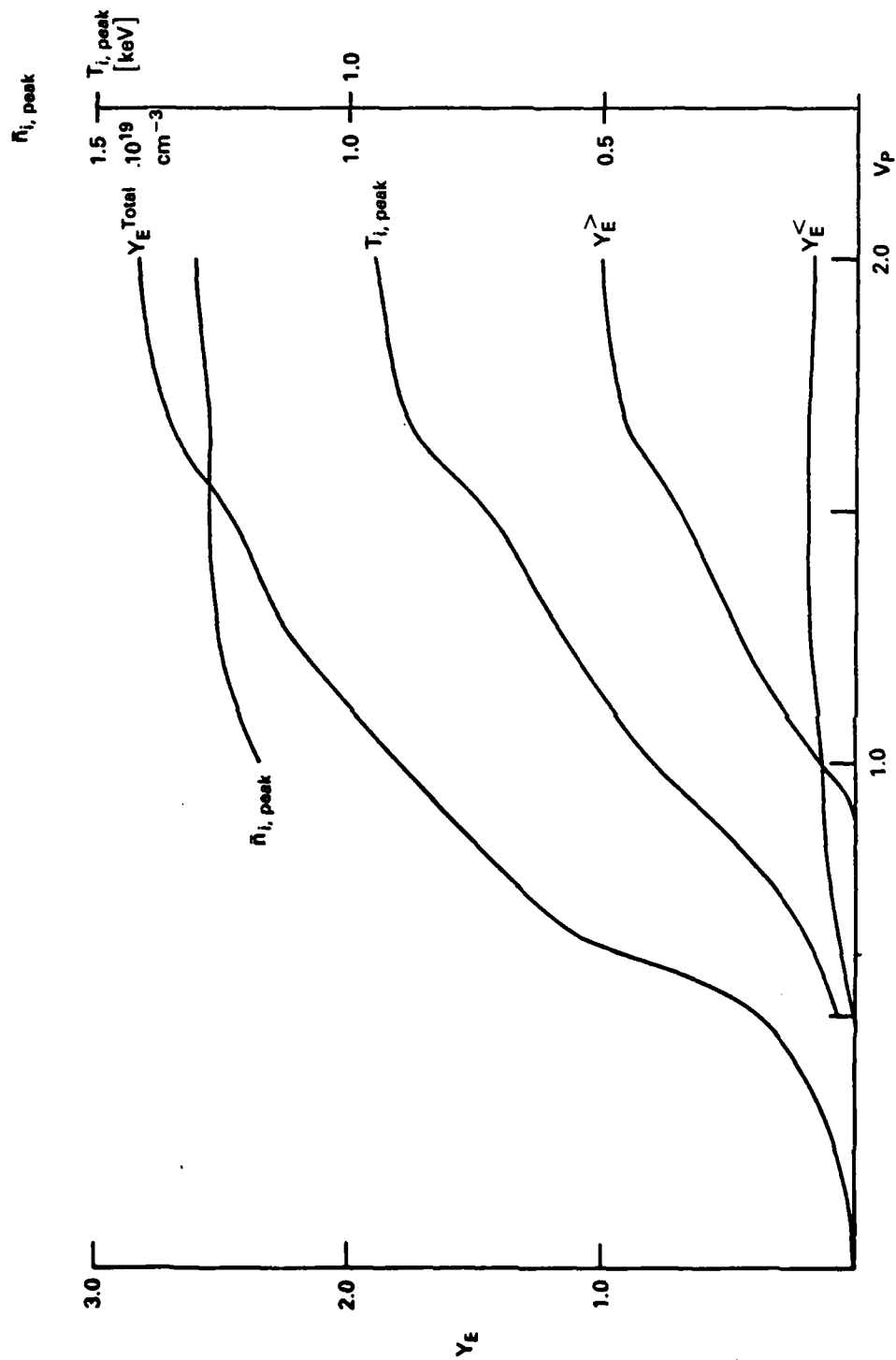


Figure 6. Yield vs. V_p (Case C12)

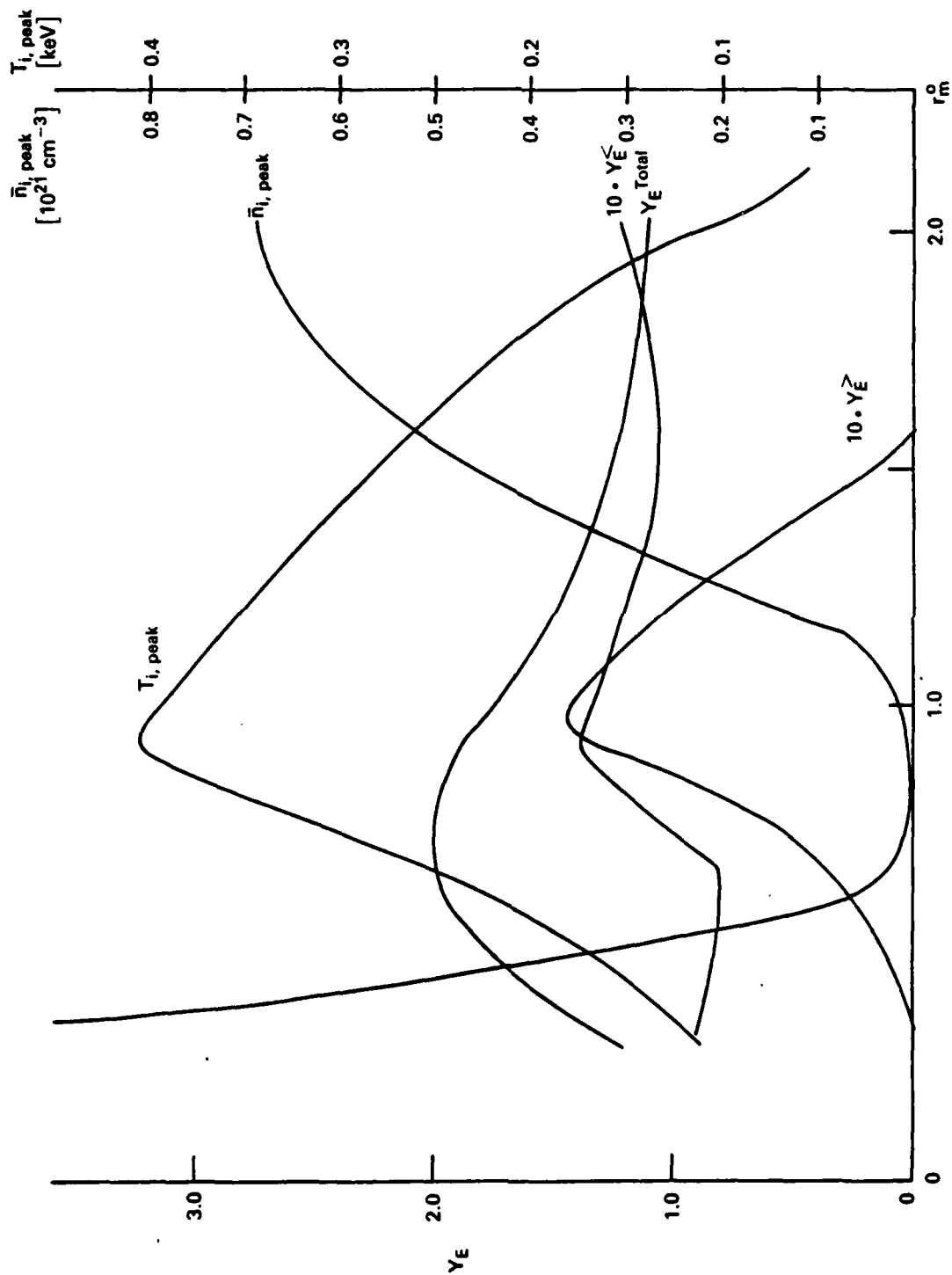


Figure 7. Yield vs. r_m^0 , fixed g_0

optimum in r_m^0 because of a combination of kinematic and dynamic effects. At large r_m^0 , even though β rises rapidly to near 0.97 from a small initial value, the load has too large a distance to cover in the fixed rise and fall time of the driving voltage. This produces the larger currents while the conductor is at larger radius and hence does not give the larger values of $J_z \times B_\theta$ that can be obtained with smaller r_m^0 . Bringing r_m^0 down thus gives a "kinematic" optimization and improves the yield, peak temperature and compression. On the other hand if r_m^0 is too small the load experiences strong inward forces but does not have enough distance of travel to allow these forces to deliver much kinetic energy. This is a dynamic degradation of the implosion quality, caused by being too close to the bottom of the effective potential well created by the generator.

Finally the variation with load mass is shown in Figure 8, generated by initial cases C6, C8, C12, C16, C24 at fixed voltage V_0 and $g = 9.0$. Also for comparison this mass variation is shown in Figure 9 with r_I fixed rather than g . In this later sequence g will change slightly at t_0 because the profiles which envelope a smaller mass do not spread as far from the peak r_m^0 as those of larger mass. Physically the sequence with fixed g corresponds to early histories which imbed the current in a fixed fraction of the load volume, while the sequence with fixed r_I corresponds to early histories that produce thinner skin depths on smaller masses due to a more rapid heating which freezes the current diffusion before it has a chance to penetrate. Dynamically the yield will degrade for both large and small masses. Large masses cannot be accelerated well and thus build no kinetic energy reservoir with which to drive the radiation. Small masses heat too rapidly and hold off the compression of the load, degrading the yield because too low a density is achieved.

Finally, in Figure 10, the variation of the yield with g is shown in order to illustrate the general sensitivity of the implosion quality to the detailed microscopic assumptions underlying the calculation of the load dynamics. Larger g values produce more rapid compressions and higher peak temperatures because they create higher surface stresses — roughly similar total currents are confined to a narrower annulus, increasing $J_z \times B_\theta$. For very large g values, of course, the core current will decay ($\beta \rightarrow 0$) because infinite current densities are not allowed due to coronal growth.

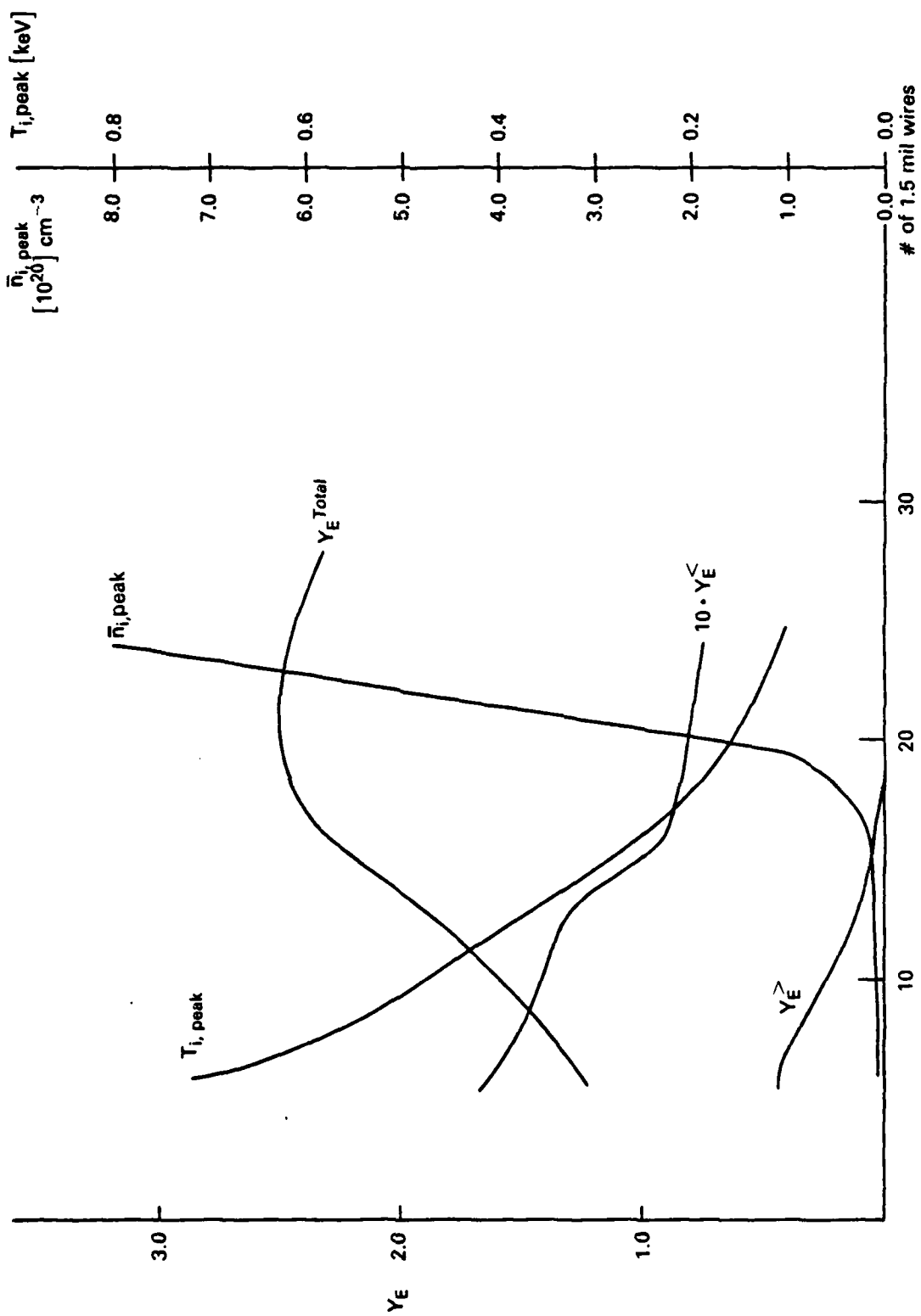


Figure 8. Yield vs. Mass, fixed g_0

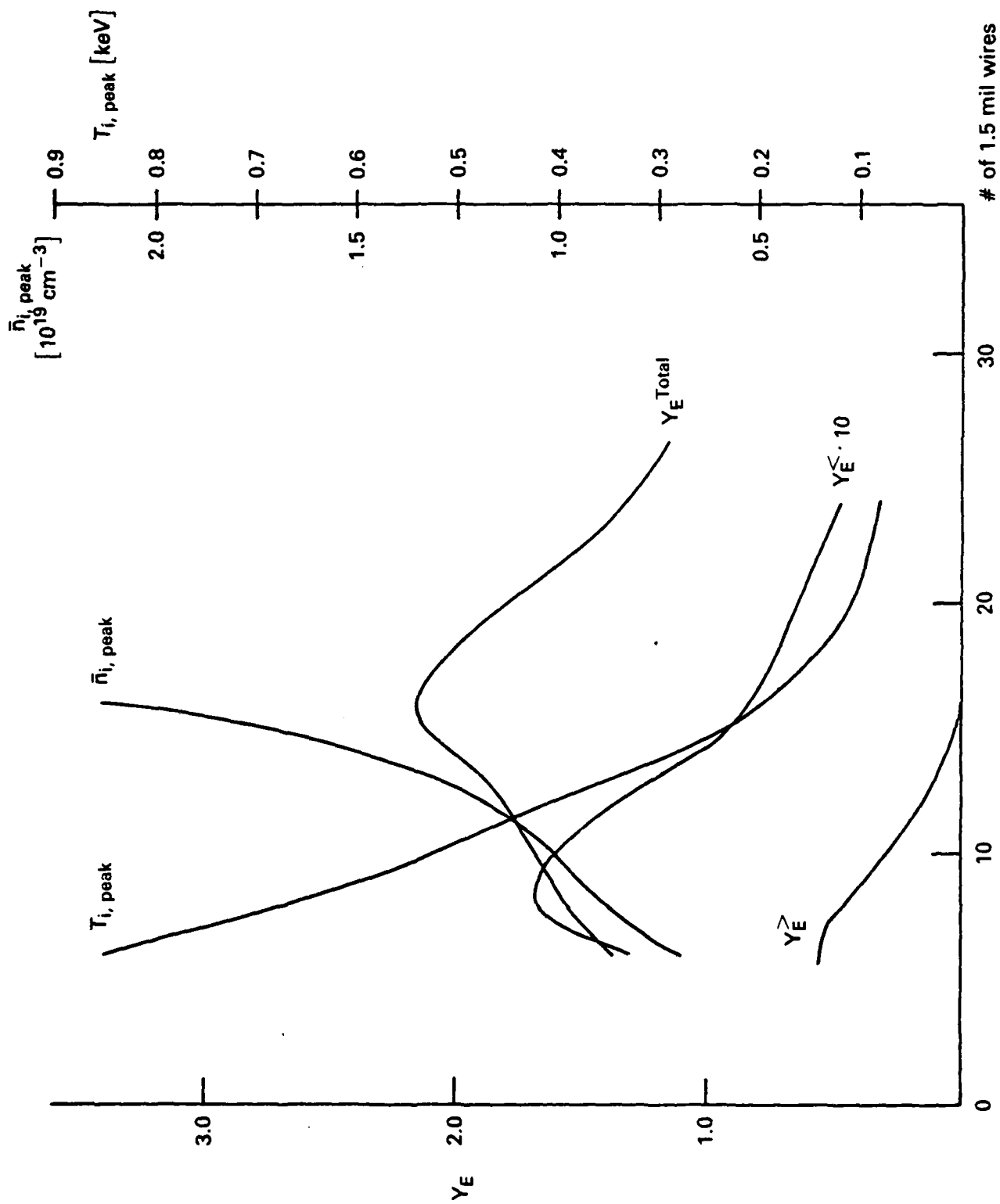


Figure 9. Yield vs. Mass, fixed r_I^0

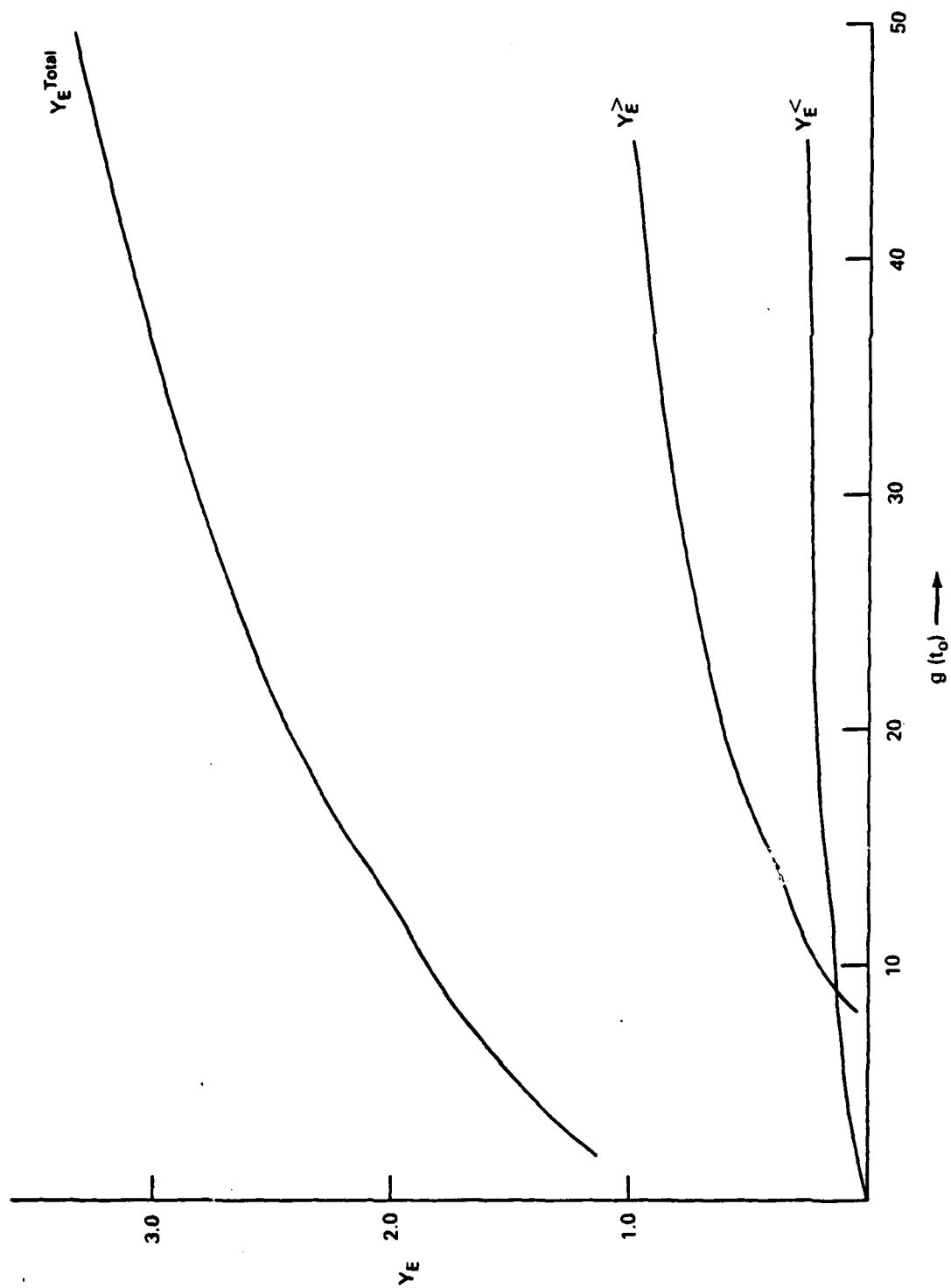


Figure 10. Yield vs. $g(t_0)$

E. Testing the Yield Dependence on a Possible Scaling Parameter

Recent Maxwell Laboratory experiments⁶ have examined the utility of the parameter $K_1 \equiv r_m^0 M_o^{1/2}$ as a measure of implosion performance. It has been shown to be a poor indicator of implosion quality—with yields decaying rapidly and peak temperatures increasing as one progresses to larger values of r_m^0 at constant K_1 . The load masses in the Maxwell experiments are smaller than those used in the studies described above, but SPLAT calculations (at the larger masses used before) indicate that K_1 fails as a measure of implosion performance for the model plasma also.

Using the standard generator impedance and inductance from Table 1 and adjusting the driving voltage waveform model for a 80 → 150 nsec rise time to a peak voltage of 1.5 → 3.0 MV, a sequence of SPLAT calculations at variable r_m^0 with fixed $K_1 \sim 17.8 \text{ [cm.}\mu\text{g]}^{1/2}$ shows a trend similar to the experimental behavior. In Figure 11 these results are shown as a function of array radius. The yield falls because of a systematic trend toward overheating at large radii, if sufficient mass is removed to hold K_1 constant. The greater temperatures reverse the implosion too soon and prevent compression to densities sufficient for appreciable radiative yield. According to the SPLAT code dynamics, the proper contour of constant yield would involve a slower power vs mass, $K \sim r_m^0 M_o^\gamma$, with $\gamma < 1/2$ in order to prevent the overheating.

This failure of K_1 to represent a figure of merit corresponding to yield Y^T or $Y^>$ is due probably to the origin⁷ in an optimization based on constant levels of power coupling from the generator to the load. Since the input power levels are only weakly related to the time integrated radiative loss, or yield, this parameter is suspect at the outset.

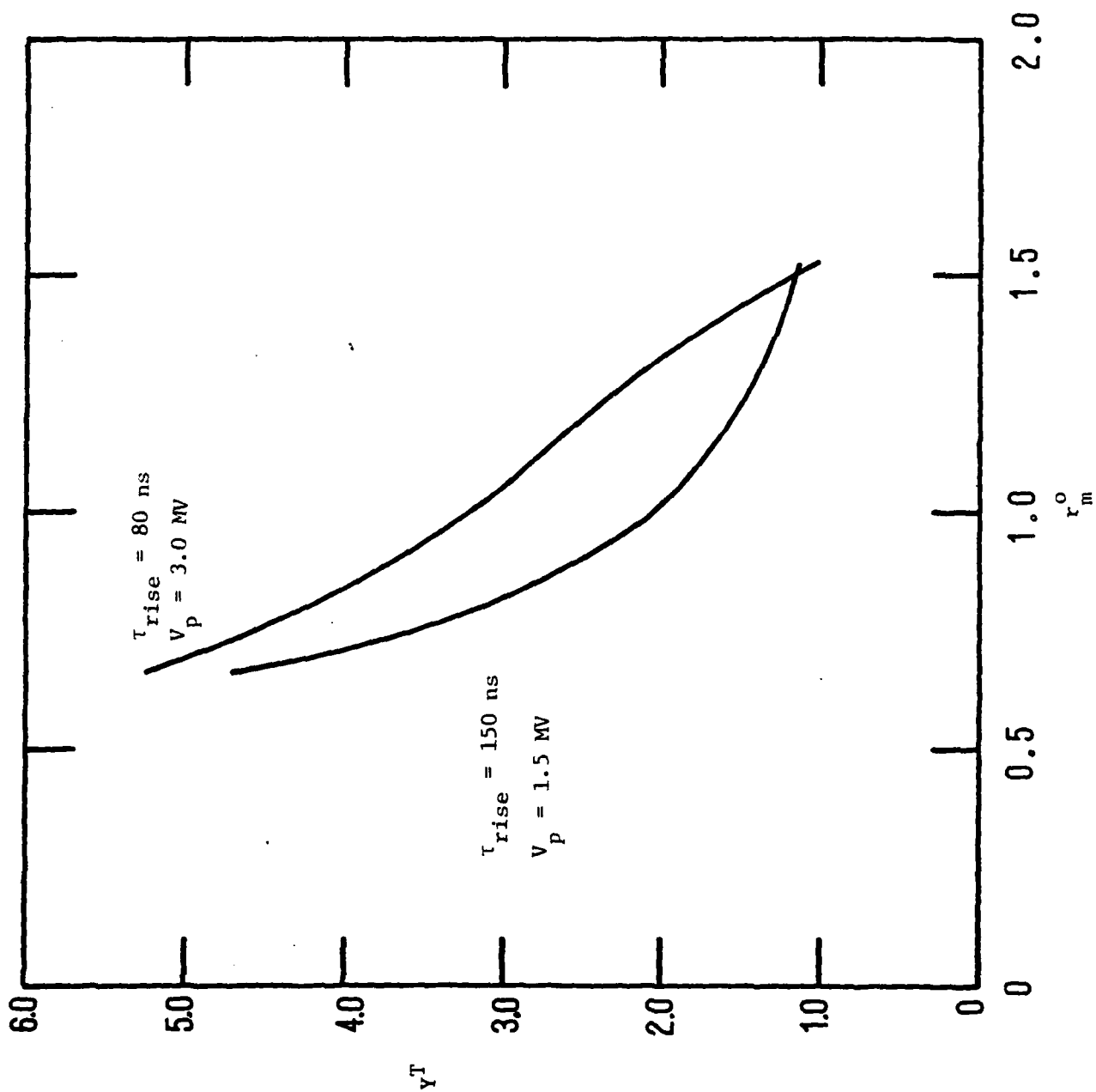


Figure 11. Total Yield as a Function of r_m^0 at Constant $K_I = 17.8 [\mu\text{g cm}]^{\frac{1}{2}}$

CHAPTER III. ELECTRODYNAMIC MODELS OF ANNULAR PLASMA LOADED DIODES BASED ON A GENERALIZED HERTZ VECTOR POTENTIAL

A. Introduction

The common use of a circuit equation (usually derived from Faraday's law) in MHD models of imploding annular plasma loads is grounded in very serious simplifications of the actual electrodynamics in pulse driven diodes. The most important simplifications involve the use of an essentially electrostatic approximation for the electric field, the use of magnetic field diffusion theory in the presence of an inhomogeneous, time varying, convecting conductor (the plasma load), and the neglect of the tensor character of the collisional plasma conductivity due to the imbedded azimuthal magnetic field. Moreover, the geometry of actual machines is complex enough to preclude detailed electromagnetic theoretical analysis in anything less than three spatial dimensions.

Many difficulties can be removed from the conventional theoretical treatments by simply insisting on a more rational diode geometry.⁸ A simpler, more z-symmetric diode feed would obviously simplify analysis and prediction of the experimental results. Significantly, the choice of new diode geometries may be guided by theoretical analysis using a generalization of the Hertz potentials^{9,10} which are intrinsically suited to the problem of fluid conducting plasma in a wave-guide. The choice of boundary conditions can select particularly simple electromagnetic field solutions and load configurations that admit a relatively tractable analysis over a rather general class of waveguide geometries and electrodynamic load properties.

The new field equations for the generalized Hertz potentials are equivalent to the Maxwell equations which give rise to them, but they are simpler in that a single vector field is derived that represents E and B. The solution of a single wave equation (or wave-diffusion equation) is then sufficient to provide all the electromagnetic field components. This new vector field $\underline{Z}(\underline{x},t)$ is equivalent to the usual Hertz vector potential only in source free regions and therefore represents a non-trivial generalization of the original field. The choice of $\underline{Z}(\underline{x},t)$ is in fact the generalization of the familiar process of making a convenient gauge choice,

allowed by the arbitrary lamellar component of the ordinary vector potential \underline{A} . Here \underline{Z} will be chosen so as to remove the need for two inhomogeneous Maxwell equations, and to replace them with a single equation to determine \underline{Z} .

B. The fundamentals Revisited

Such a program of reduction can always be carried out when the field sources are prescribed functions, i.e., $\rho = \rho(\underline{x}, t)$, $\underline{J} = \underline{J}(\underline{x}, t)$ are given and the fields external to these sources are required. In this case one must seek a vector potential $\underline{Z}(\underline{x}, t)$ which

- (i) allows the definition $\phi(\underline{x}, t) = -\underline{\nabla} \cdot \underline{Z}(\underline{x}, t)$ to represent a gauge choice relating ϕ , $\underline{A}(\underline{x}, t)$ (the usual vector potential) and,
- (ii) reduces the number of inhomogeneous field equations from two (for ϕ and \underline{A} separately) to one for the new potential \underline{Z} .

Performing the usual elimination of the homogeneous Maxwell equations by introducing ϕ and \underline{A} , the two remaining relations become

$$\underline{\nabla} \cdot (\underline{\nabla} \phi + c^{-1} \partial_t \underline{A}) = -4\pi \rho \quad (4a)$$

$$\underline{\nabla} \times \underline{\nabla} \times \underline{A} + c^{-1} \partial_t (\underline{\nabla} \phi + c^{-1} \partial_t \underline{A}) = +4\pi c^{-1} \underline{J}. \quad (4b)$$

Now choose the generalized Hertz vector \underline{Z} so that

$$\underline{A} \equiv c^{-1} \partial_t \underline{Z} \quad (5)$$

and if $\phi \equiv -\underline{\nabla} \cdot \underline{Z}$ then a familiar gauge choice ($\underline{\nabla} \cdot \underline{A} + c^{-1} \partial_t \phi = 0$) is implied. If one now replaces ϕ and \underline{A} in (4a, b) with the equivalent \underline{Z} terms, the equations become

$$\square^2(\underline{\nabla} \cdot \underline{Z}) = 4 \pi \rho \quad (6a)$$

$$\partial_t \square^2 \underline{Z} = -4 \pi \underline{J}. \quad (6b)$$

The procedure for choosing \underline{Z} is formalized in Appendix A, which points out the role of a Hertz vector potential in the conventional electrodynamics.

Let the source field \underline{J} be represented by the time derivative of the charge transferred per unit area in any spatial direction over the entire time domain of interest, viz.

$$\underline{J} = \partial_t \underline{T}(\underline{x}, t), \text{ or} \quad (7)$$

$$\underline{T} \triangleq \int^t dt \underline{J}(\underline{x}, \tilde{t}) + \underline{T}^0(\underline{x}).$$

Using the continuity relation, it is easily shown that $\underline{T}(\underline{x}, t)$ reduces the problem to a single wave equation

$$\square^2 \underline{Z} = -4 \pi \underline{T}, \quad (8)$$

because (6a) is subsumed in the divergence of (8) so long as $\underline{T}^0(\underline{x})$ is a solenoidal field. In terms of the potential \underline{Z} and transfer vector \underline{T} , the observable fields are written

$$\underline{E} = \underline{\nabla} \times \underline{\nabla} \times \underline{Z}(\underline{x}, t) - 4 \pi \underline{T} \quad (9)$$

$$\underline{B} = c^{-1} \underline{\nabla} \times \partial_t \underline{Z}(\underline{x}, t) \quad (9b)$$

and the uniqueness of $\underline{Z}(\underline{x}, t)$ is guaranteed because the specification of ρ or \underline{J} , i.e. $\underline{T}(\underline{x}, t)$, and the initial fields $\underline{E}(\underline{x}, t_0)$, $\underline{B}(\underline{x}, t_0)$ at some time t_0 , can be seen to imply Cauchy open-surface boundary conditions for the wave equation (8). The uniqueness of \underline{Z} is also discussed in Appendix A.

In a waveguide formed by two infinite plane parallel perfectly conducting surfaces, the Hertz vector \underline{Z} represents a variety of electromagnetic wave solutions. However, given the azimuthal symmetry and perfectly conducting guide surfaces, only a particular subset are of interest in analyzing and describing the evolution of an annular plasma load. One seeks radially varying TEM modes which limit asymptotically as $r \rightarrow \infty$ to a superposition of incoming and outgoing cylindrical waves with (perhaps) a quasi-static component added. At large radius, the vacuum/waveguide boundary conditions therefore restrict consideration to those solutions

$$\underline{Z} = \hat{z} \left\{ \zeta^t(r, t) + \zeta^l(z, t) \right\} \quad (10)$$

where t, l denote the solenoidal and lamellar portions of the Hertz vector. The radial component of \underline{Z} must vanish because if one insists that the scalar potential ($-\nabla \cdot \underline{Z}$) exhibit no radial gradients (in consonance with the boundary conditions), then the \underline{E}_r arising from the solenoidal portion of \underline{Z} can vanish if and only if \underline{Z}_r itself is everywhere zero.

The delicate question is how to preserve this solution as it collides with and is reflected by a convecting quasineutral ($\rho \approx 0$) plasma load which exhibits strong conductivity gradients. The plasma must possess and self-consistently retain several symmetries in order to insure retention of \underline{Z} in the form given above. The central requirement is that \underline{E} be orthogonal to $\nabla \sigma$. Since \underline{E} arises from the independent fields ϕ and \underline{A} , it is sufficient to require that ϕ have no radial gradients and that

$$\underline{\nabla} \times \underline{\nabla} = 0, \quad (11a)$$

$$\underline{\nabla} \times \underline{\nabla} \sigma = 0, \quad (11b)$$

$$\sigma \underline{\nabla} \cdot \underline{\nabla} \times \underline{\nabla} \times \underline{A} = 0, \quad (11c)$$

where one has in the rest frame of the convecting plasma (superscript ')

$$\underline{J}_\perp = \underline{J}_\perp' = \sigma(\underline{x}, t) \gamma(\underline{V}(\underline{x}, t)) \left\{ -\underline{\nabla} \phi - c^{-1} \partial_t \underline{A} + \frac{\underline{V}}{c} \times \underline{\nabla} \times \underline{A} \right\},$$

orthogonal to the gradients of $\sigma(\underline{x}, t) \equiv \sigma(\underline{x}, t) \gamma(\underline{V}(\underline{x}, t))$ and to the convection field $\underline{V}(\underline{x}, t)$.

The next step is to try to carry out the program used above when ρ and \underline{J} were given functions. In this case the choice of $\underline{Z}(\underline{x}, t)$ is not so transparent; one must construct the proper functional $\underline{A}(\underline{Z})$ which provides the results (i) $\phi = -\underline{\nabla} \cdot \underline{Z}$, and (ii) only one (in this case homogeneous) propagation equation is non-trivial. Such a construction can be done using the Green's function solution of

$$\nabla_{\underline{x}}^2 G(\underline{x}, \underline{\tilde{x}}) = -4\pi\delta(\underline{x} - \underline{\tilde{x}})$$

which provides the proper boundary conditions in the waveguide. For the plane parallel perfect conductors and the axially independent cylindrical wave solution at large radius, this requires $G(\underline{x}, \underline{\tilde{x}}) = G(r, \tilde{r}, \theta - \tilde{\theta})$, a single line source located at $(\tilde{r}, \tilde{\theta})$; but the method outlined in Appendix B is applicable in any geometry.

The solution algorithm for $\underline{A}(\underline{Z})$ and \underline{Z} (as discussed in Appendix B), uses the mathematics of space-ordered exponential operators, and appears to provide a relatively straightforward computational means of solving the otherwise-intractable problem of fields in the presence of a convecting inhomogeneous plasma load with time-varying conductivity. As long as the diode surfaces are approximated as perfectly conducting, the solution demands (TEM) modes governed by a single transverse component of the vector \underline{Z} , i.e. $\zeta^{\perp} \rightarrow 0$ everywhere. When the perfectly conducting waveguide and the plasma are configured such that (a) radial plasma convection currents are divergenceless (i.e., plasma waves in the ambipolar space charge can be neglected), (b) the plasma gradients are radial, and (c) the plasma is axially uniform, then all axial load currents and radial guide surface currents are given in terms of E and B fields derived from the transverse axial component of the generalized Hertz vector, $\underline{Z} = \hat{z}\zeta(r, t)$.

The next step in a complete plasma/diode model is the constitutive relation $\underline{j} = \sigma \underline{E}$. The Braginskii transport coefficients express currents in the plasma load in terms of the fields, and the result can be interpreted as

requiring (a) radial force balance on an "average electron" which responds to the space-charge field E_r created by pressure gradients and axial current, and (b) constant axial electron drift speed on the electron-inertia timescale, i.e., adiabatic axial electron currents, changing on the slower timescale of the fields. Assuming that the axial drift speed (J_z/ne) and the radial stress quickly relax to quasi-equilibrium on timescales fast compared with those for field changes, one can make a fully self-consistent treatment of the evolution of the radial fluid velocity $V_r(r,t)$, axial current density $J_z(r,t)$ and the incident electromagnetic field $Z(r,t)$ simultaneously. The details are discussed in Appendix C.

The theory developed above is an adequate basis for the proper calculation of the field/plasma momentum exchange in any radial implosion whenever the conductivity relation is scalar and linear. In the classical, weakly coupled plasma of course this relation is not strictly scalar, but to a good approximation the tensor character of the Ohms law can be superimposed on the electromagnetic field picture developed above as a quasi-static perturbation. The new field component which must arise (within the plasma load) is an ambipolar radial E field due to radial pressure gradients, Hall effects, and thermo-electric effects. In the present case this radial field will be independent of axial coordinate and will vanish in the vacuum region of the waveguide because it is essentially the field of a radially varying axially uniform line image charge $Q_I(r)$ with $Q_I(r) \rightarrow 0$ as $\sigma(r,t) \rightarrow 0$ in r . Using the radial stresses developed from both $\rho E_r|_{\text{ambipolar}}$ and $\sigma E_z \times B_0$ one can therefore define a completely self-consistent momentum transfer between the far waveguide electromagnetic field and the annular plasma load. The result will be a more definitive picture of the load dynamics than has been possible heretofore in the classical weak coupled plasma limit. This detailed model will be developed further in Section E, but a simple illustration of the physical content of this vector $Z(r,t)$ will serve to motivate that analysis.

C. Simple Solutions in the Steady State Plane Parallel Waveguide

In the case of steady fields the solution for $Z(r,t)$ assumes a quite symmetric form which can be seen to be a firm time asymptotic limit of the solutions to the complete wave equation B8. Consider a constant

conductivity (σ_0), immovable ($V_r \rightarrow 0$), plug ($r < r_p$) in the plane parallel waveguide and transform B8 using the dimensionless variables

$$\begin{aligned} x &= r/r_0, \\ \tau &= ct/r_0, \\ \Sigma_0 &= r_0 \sigma_0 / c, \end{aligned} \quad (12)$$

based on an arbitrary scale radius r_0 , which can be conveniently set as r_p . The integrations over the conducting region produce two wave equations with continuous sources on the domains

$$\begin{aligned} x > 1: \quad x^{-1} \partial_x x \partial_x Z - \partial_\tau^2 Z &= 4\pi \ln x \partial_\tau \left[\Sigma_0 (x \partial_x Z)_{x=1} \right] \text{ and} \\ x \leq 1: \quad x^{-1} \partial_x x \partial_x Z - \partial_\tau^2 Z &= 4\pi \left(\partial_\tau \left[\Sigma_0 Z(x, \tau) \right] - \partial_\tau \left[\Sigma_0 Z(1, \tau) \right] \right). \end{aligned} \quad (13)$$

The steady E_z , B_θ fields available to this system are described by Z fields which arise as solutions to the homogeneous wave equation. The usual vector potential $A_z(x, \tau)$, cf B9b, exhibits a clear decomposition into E_z terms and B_θ terms, which eliminates the scalar potential entirely as previously anticipated. In particular one has

$$\begin{aligned} Z(x, \tau) &= Q_0 \left(\frac{\tau^2}{2} + \frac{x^2}{4} \right), \text{ with} \\ (x > 1) \quad A_z^>(x, \tau) &= r_0^{-1} Q_0 (\tau + 2\pi \Sigma_0 \ln x), \\ B_\theta^>(x, \tau) &= - \left[2\pi \Sigma_0 Q_0 / r_p^2 \right] x^{-1} \equiv \frac{2I(r_p)}{cr}, \\ (x < 1) \quad A_z^<(x, \tau) &= r_0^{-1} Q_0 (\tau + \pi \Sigma_0 (x^2 - 1)) \\ B_\theta^<(x, \tau) &= - \left[2\pi \Sigma_0 Q_0 / r_p^2 \right] x \equiv \frac{2I(r < r_p)}{cr}, \end{aligned} \quad (14)$$

and $E_z = -Q_0/r_0^2$ everywhere. The fields here corresponding to those of a leaky capacitor with a constant voltage source at $x \rightarrow \infty$ maintaining a steady voltage.

The potential clearly decomposes into a space-like component, x^2 , and a time-like component, τ^2 . The space-like function represents the charge contained at any time within the radius x on the waveguide plane, while the time-like function represents the cumulative charge involved in the continuous superposition of incoming and outgoing TEM waves which add up to the steady, uniform vector field E_z . The ordinary vector potential A_z also exhibits this type of decomposition, with a continuous value and spatial derivative at the conducting interface $x = 1$. In contrast to a more conventional formulation of the same problem using distinct scalar and vector potentials, the present method makes a smooth transition to the time dependent problem posed by time variations in either Σ_0 or $E_z|_{x \rightarrow \infty}$. In these situations the source terms are forced to be non-zero because $\partial_\tau(\Sigma_0 Z)$ cannot remain spatially independent and accommodate the boundary conditions. Outside $r_p(x > 1)$, the time dependent value of $\Sigma_0(x \partial_x Z)|_{x_0=1}$ spawns outward running waves which communicate changes in the conductor to the charge distributions on the guide planes. Inside the value of $\Sigma_0 Z$ at the interface ($x_p=1$) acts as a source of damped waves which continue to penetrate the conductor by propagation and diffusion until a uniform E_z (free wave) solution is again established at some new boundary value $E_z|_{x \rightarrow \infty}$. Treating the same or a similar problem using a separate set of A, ϕ this simple process of charging the capacitor or changing the conductivity requires some connection between the two potential functions in order that B_θ, E_z become properly interdependent. Such a connection, or the complete elimination of ϕ , is not always transparent and the present Hertz vector formalism achieves this elimination quite easily.

It might appear a viable conjecture that such symmetry breaking as seen in the time dependent "leaky capacitor" problem, the destruction of the space-like plus time-like Hertz potential solutions, is a fundamental property of the theory. This is in fact the case, as discussed in the following section.

D. Explicit Source Transformations of the Wave Equation and the Separation of Time Scales

The homogeneous relation (B8) which specifies the evolution of $Z(r,t)$ can be simplified considerably at the expense of introducing a manifestly physical but somewhat complicated source term involving the current density profile of the plasma. Again, setting the equation in dimensionless variables and choosing an (arbitrary) dimensionless scale radius x_N in the static Greens function (a radius sufficient to contain the bulk of the load mass, for example), the terms of B8 which contain all of the source information exhibit the following identity

$$\begin{aligned} \tilde{\Sigma}Z + \int_x^\infty d\tilde{x} Z \cdot \partial_{\tilde{x}} \tilde{\Sigma} - \int_x^\infty d\tilde{x} \partial_{\tilde{x}} \tilde{\Sigma} \tilde{x} \ln\left(\frac{\tilde{x}}{x_N}\right) \partial_{\tilde{x}} Z - \ln\left(\frac{x}{x_N}\right) \cdot \int_0^\infty d\tilde{x} (\partial_{\tilde{x}} \tilde{\Sigma}) (\tilde{x} \partial_{\tilde{x}} Z) \\ = - \int_0^\infty d\tilde{x} \tilde{x} \ln\left(\frac{\tilde{x}}{x_N}\right) \tilde{\Sigma}(\tilde{x}, \tau) \mathcal{E}^0(\tilde{x}, \tau), \end{aligned} \quad (15)$$

where $\mathcal{E}^0 = -x^{-1} \partial_x x \partial_x Z$ and $x^>$ is the greater of x , \tilde{x} . When this result is combined with the $c^{-1} V_r(\tilde{x}, \tau) (\equiv \beta_r)$ convection terms a simple, very physical statement obtains

$$\partial_\tau^2 Z - x^{-1} \partial_x (x \partial_x Z) = 4\pi \partial_\tau \left[\int_0^\infty d\tilde{x} \tilde{x} \ln\left(\frac{\tilde{x}}{x_N}\right) \tilde{\Sigma}(\tilde{x}, \tau) \hat{\mathcal{E}}(\tilde{x}, \tau) \right] \quad (16)$$

where $\hat{\mathcal{E}} = \mathcal{E}^0 - \beta_r \partial_x \left[\partial_\tau Z - 4\pi \int_0^\infty d\tilde{x} \tilde{x} \ln\left(\frac{\tilde{x}}{x_N}\right) \tilde{\Sigma} \mathcal{E}^0 \right]$ is the (dimensionless)

representation of the field E'_z in the convecting frame β_r . The generalization to all orders in β_r is quite straightforward (and generates the space ordered exponential series discussed in Appendix B), but it is not required when the convection speed implies $\beta_r \ll 1$, as is usually the case in experimental situations of interest. This new relationship displays quite vividly the conjecture of the previous section. The source term is always zero in any situation where $\tilde{J} \equiv \tilde{\Sigma} \hat{\mathcal{E}}$ is time independent (for any spatial configuration of the conductivity $\tilde{\Sigma}$) and thus only temporal variations in J can force solutions for $Z(x, \tau)$ which depart from the simple

form seen in the previous section after a light transit time across the radial domain of interest.

A second result of (16) above is that a clear separation of the time scales occurs. The free wave solution, being characterized by the light transit time across the system, will respond to the much slower time variations of the source term by simply propagating variations in \mathcal{E}^0 and \tilde{J} over the system. In any numerical scheme designed to solve (16) it is therefore essential to find some means to calculate this propagation over large intervals in τ , and allow a concentration of the numerical effort on tracking the temporal variations of the source. In Appendix D an explicit forward quadrature for the free wave propagation is developed which removes this problem. The method is related to the Poisson integral representation of two dimensional wave solutions, but it is developed directly from the free wave Greens function in two spatial dimensions.

The result of each forward quadrature is the specification of $Z(x_j, \tau_{i+1})$ and $\partial_{\tau_{i+1}} Z(x_j, \tau_{i+1})$ on a specified (easily rezonable) mesh; and these values are, of course, sufficient to specify all the sources required to compute the next forward step once the temporal and spatial variation of $\beta_r, \tilde{\Sigma}$ is known. In the fully self-consistent formulation the evolution of $\beta_r, \tilde{\Sigma}$ is provided by a similar forward advance of hydrodynamic plasma variables, but the method developed in Appendix D allows any source of these fields. The development of the Hertz vector sources, on the right of (16) above, can be cast in a relatively compact set of operations which proceed from ${}^i Z_j, \partial_{\tau} {}^i Z_j$ and use the wave equation itself to eliminate higher order time derivations of Z when they appear in $\partial_{\tau} \hat{\mathcal{E}}, \partial_{\tau}^2 \hat{\mathcal{E}}$, etc.

E. The 1-D Electromagnetohydrodynamic Model for the Plane Parallel Waveguide

In the numerical method a more natural variable is $a = x^2$ since this removes some coefficients in the differential operators which are singular at $x \rightarrow 0$. The variables a and x are used interchangeably in the following discussion; and Q_0 is a reference charge value which allows Z to be dimensionless as well. Any forward advance of the system must begin with a specification of ${}^i Z_j \equiv Z(x_j, \tau_i)$ and ${}^i \dot{Z}_j \equiv \partial_{\tau_i} Z(x_j, \tau_i)$ together with the plasma state variables

$$n_I(x_j \tau_i), \mathcal{F}(x_j \tau_i), \varepsilon_I(x_j \tau_i), T(x_j \tau_i), \beta_r(x_j \tau_i),$$

the ion density, ionization state, chemical potential, electron and ion temperature, and radial convection field.

These fluid variables and their gradients provide the values of \dot{n}_j , \dot{n}_j required to calculate $\partial_{\tau} \tilde{\Sigma}$ and its higher time derivatives; the Hertz field variables \dot{z}_j and \dot{z}_j provide the required input to compute $\partial_{\tau_i} \hat{\mathcal{E}} \equiv \dot{\mathcal{E}}_j$ and its higher time derivatives. For example, the systematic specification of the time derivatives of $\hat{\mathcal{E}}$ requires

$${}^i \mathcal{E}_j = -4 (\partial_a a \partial_a {}^i z)_j, \text{ or } E_z = -Q_0 r_0^{-2} \mathcal{E} \text{ in lab coordinates,}$$

$${}^i \hat{\mathcal{E}}_j = -2a^{1/2} {}^i \beta_j \left[(\partial_a {}^i \dot{z})_j - \frac{\pi}{a_j} \int_0^{a_j} da_1 [\tilde{\Sigma} \mathcal{E}]_{a_1 \tau_i} \right] + {}^i \mathcal{E}_j$$

$${}^i B_j = -2a^{1/2} \left[(\partial_a {}^i \dot{z})_j - \frac{\pi}{a_j} \int_0^{a_j} da_1 [\tilde{\Sigma} \hat{\mathcal{E}}]_{a_1 \tau_j} \right] \quad (17)$$

$${}^i \dot{\mathcal{E}}'_j = -4 (\partial_a a \partial_a {}^i \dot{z})_j - 2a^{1/2} {}^i \beta_j (\partial_a^2 a \partial_a {}^i z)_j - {}^i \dot{\beta}_j \cdot 2a^{1/2}.$$

$$\left[(\partial_a {}^i \dot{z})_j - \frac{\pi}{a_j} \int_0^{a_j} da_1 [\Sigma \mathcal{E}]_{a_1 \tau_i} \right]$$

•
•
•

and these in turn specify, when $\partial_{\tau} \Sigma$ is included, the complete source term for the next time advance of Z , \dot{Z} , viz.

$$\frac{1}{4} \int_0^{\infty} da_1 \ln \left(\frac{a}{a_N} \right) \partial_{\tau_i} [\tilde{\Sigma} \hat{\mathcal{E}}]_{a_1 \tau_i}.$$

From these same fields the fluid stress, which provides β_j , can be calculated from the formulation in Appendix C and the implied $j \times B$ force density —

$$- q_0 r_0^{-5} [\tilde{\Sigma} \hat{E} B]_{a_j \tau_1}.$$

The external voltage source can be modeled by enforcing a boundary value for \hat{E} at some large radius (as a function of time) and the current drawn by the model plasma is simply the spatial integral of $\tilde{\Sigma} \hat{E}$ over the domain. Drift speed limits on current conduction can be imposed quasi-statically at every time step in much the same manner as one develops the Braginskii conductivity in Appendix C. As the plasma density falls, with \hat{E} given, there will always exist some radius for which the drift speed u_z will be forced to exceed the sound speed c_s , and this will define implicitly a (nonlinear) conductivity $\tilde{\Sigma}(\hat{E})$ which satisfies the constraint $j_0 \tilde{\Sigma}(\hat{E}) \cdot \hat{E} = e z n_I c_s$. In practice this limitation may drift in or out in x as the \hat{E} profile develops and it will generalize the present SPLAT coronal region in a quite physical manner.

The calculation of the usual classical heat sources and the radiative losses can be folded into the model as further fluid source terms in any of a variety of well known methods based on previous work.

CHAPTER IV. IMPLICATIONS OF DISCHARGE BEADING WITH LOW-DENSITY INTERCONNECTION REGIONS

Introduction

The late-time, fully-developed stage of sausage-like "beading" of z-pinch discharges can give rise to enhanced electron heating (and thus enhanced radiative losses), caused by Ohmic anomalous heating in the constricted regions. In this chapter this transfer of energy from condensations of magnetic field energy to radiation is examined quantitatively, based on assumptions about the nonlinear state of the instability.

Constricted portions of the discharge, with low density and cross-section, and mostly or entirely "anomalous" current, alternate with the higher density "beads", which carry current classically. The extreme limit of this phenomenon is that of multiple diodes in series, with the nearly-evacuated low density regions considered as bipolar-flow diodes, with pinched electron flow, as suggested by Goldstein¹¹. In all probability, the low-density regions cannot evacuate to the extent required for such vacuum-diode behavior.

The overall resistive heating rate is of course VI , with the total current I given by appropriate circuit equations, but the local heating rates for electrons in the low density regions are balanced by increased radiative loss when these hotter electrons collide with the denser blobs of plasma. The blobs cannot respond hydrodynamically to the increased heating before radiation loses the deposited energy.

Current

We first examine the conditions under which all the current in the low-density regions would be drift-speed limited, i.e., (approximately) when the classical drift speed $v_d = \sigma E / n_e e$ would exceed the sound speed c_s . From $\sigma_{\perp} = \omega_p^2 / 4\pi \nu_{ei}$ and

$$v_{ei}(\text{sec}^{-1}) = 0.9 \times 10^{11} \left(\frac{\ln \Lambda}{10} \right) \left(\frac{z}{10} \right)^2 \left(\frac{n_i}{10^{18}} \right) T_{\text{keV}}^{-3/2} \quad (18)$$

we get

$$v_d(\text{cm/s}) = 1.8 \times 10^{10} \left(\frac{10}{\ln \Lambda} \right) \left(\frac{10}{z} \right)^2 \left(\frac{10^{18}}{n_i} \right) T_{\text{keV}}^{3/2} E(\text{MV/cm}) \quad (19)$$

where z is the degree of ionization ($n_e = z n_i$), σ_{\perp} is the axial conductivity, (across magnetic field lines) and $\ln \Lambda$ is the plasma parameter. The classical drift speed rises rapidly with T_e as the plasma becomes less collisional.

This is to be compared with

$$c_s = 2.24 \times 10^7 \left(\frac{26}{A} \frac{z}{10} \right)^{1/2} T_{\text{keV}}^{1/2} \quad (20)$$

For 10-times ionized aluminum ($A = 26$, $z = 10$), one sees that with electrons at keV temperatures the classical drift speed greatly exceeds the sound speed for MV/cm fields unless n_i is of order 10^{21} cm^{-3} or greater. Elsewhere we argue that the actual drift speed cannot much exceed the sound speed, so that the current is drift-speed limited to a value approximately

$$I_a(\text{MA}) = 0.36 \left(\frac{26}{A} \right)^{1/2} \left(\frac{z}{10} \right)^{3/2} \left(\frac{n_i}{10^{18}} \right) T_{\text{keV}}^{1/2} \left(\frac{\pi r_a^2}{1 \text{ mm}^2} \right) \quad (21)$$

in the anomalous ("a") low-density regions of cross-sectional area πr_a^2 . Since the current density is divergenceless, this must be the current in the circuit.

Voltage Drop in Low Density Regions

We now envision a number N of such millimeter size low-density "anomalous" regions of length ℓ_a alternating with denser "classical" regions ("beads") of length ℓ_c . Each "classical" region has, in general, a core which carries no current because it has not been penetrated by the magnetic field (and hence has no inductive E), a classical skin current layer, and an "anomalous" (drift-speed limited) outer corona. The electrical load is thus envisioned as a transmission line consisting of N elements in series, with each element as in Figure 12. Since the total current is divergenceless, it is given by Eq.(21), and depends on the applied voltage only through the temperature. If the corona carries only a small fraction ($1-\beta \ll 1$) of the current, the DC voltage drop along each classical bead is $R_c I$ where R_c is the classical resistance of the bead,

$$R_c = \frac{\ell_c}{\pi(r_c^2 - r_i^2)\sigma}$$

$$\text{i.e. } R_c (\Omega) = 3.5 \times 10^{-4} \left(\frac{z}{10}\right) \left(\frac{\ell_n \Lambda}{10}\right) \frac{\ell_c (\text{mm})}{\pi(r_c^2 - r_i^2) (\text{mm}^2)} T_{\text{keV}}^{-3/2} \quad (22)$$

with r_c the bead radius and $r_i (< r_c)$ the current penetration radius.

One can see that when inductive (LI and $\dot{L}I$) effects are small (i.e., if $\dot{L} \approx 0$ when I peaks or dips), the classical resistance of a few tens of 1 mm beads at roughly 1 keV is quite small if the current penetrates the beads, and almost all the voltage drop occurs in the anomalous regions. On the other hand, r_i/r_c tends to be frozen in at early times by the formation of the high conductivity, and tends to have values of order 10^{-1} or less, so the resistance is larger than the current-penetrated value by an order of magnitude or more. Still, this gives only a small resistance for the "classical" portion of the circuit and most of the DC voltage drop would occur in the anomalous regions.

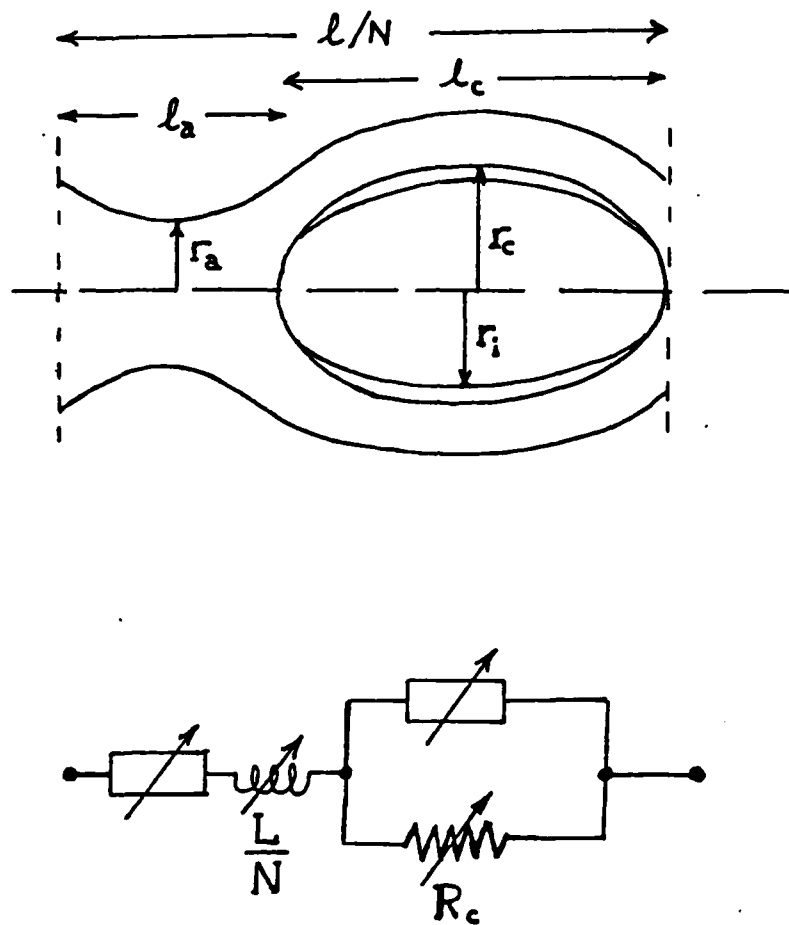


Fig. 12. Geometry and circuit model for one element of a beaded discharge. Rectangular boxes signify current limiters.

Joule Heating

Setting aside for now the question of inductive corrections, this allows us to estimate the Joule heating rate in the anomalous regions in the DC case:

$$E \cdot I = \frac{VI}{N_a \ell_a} - \frac{N_c \ell_c}{N_a \ell_a} R_c I^2 \quad (23)$$

where the last term is neglected and where I is given by Eq. (4). If all this energy went into electron temperature and none escaped to ions or photons, it would correspond to a rise

$$\dot{T} = \frac{2}{3} \frac{VI}{N_a \ell_a} \frac{1}{\pi r_a^2 z n_i} \quad (24)$$

$$\text{i.e., } \dot{T}(\text{keV/ns}) \approx 15 \text{ V(MV)} \left[\frac{1}{N_a \ell_a (\text{cm})} \right] \left(\frac{26}{A} \frac{z}{10} \right)^{\frac{1}{2}} T_{\text{keV}}^{\frac{1}{2}}, \quad (25)$$

a number of order 15 keV/ns.

The transit time of a typical electron from one bead to the next at a constant sound speed $c_s(T_{\text{keV}})$ would be

$$\tau = \ell_a / c_s = 4.5 \times 10^{-9} \text{ sec} \times \ell_a (\text{mm}) \left(\frac{A}{26} \frac{10}{z} \right)^{\frac{1}{2}} T_{\text{keV}}^{-\frac{1}{2}} \quad (26)$$

or a few ns, so that an electron could acquire several tens of keV before plowing into the adjacent dense bead and losing its energy to dense-plasma thermal energy and not-so-cold-target bremsstrahlung. In fact, a certain amount of this energy is lost to ions and radiation during transit across the anomalous region, and we now give estimates showing that loss to be dominated by classical heat conduction.

Cooling Rates Offsetting Joule Heating

The classical collisional electron cooling time to ions of atomic mass A (taken from Book, 1980) is

$$\dot{T}(\text{keV/ns}) \approx - 3.6 \times 10^{-2} \left(\frac{z}{10}\right)^2 \left(\frac{\ln \Lambda}{10}\right) \left(\frac{26}{A}\right) \left(\frac{n_e}{10^{19}}\right) T_{\text{keV}}^{-1/2} \quad (27)$$

which is negligible at 1 keV and above (unless $n_e > 10^{21} \text{ cm}^{-3}$). The radiative cooling gives approximately

$$\dot{T}(\text{keV/ns}) \sim - 4.4 \times 10^{-2} T_{\text{keV}}^{-1} \left(\frac{n_i}{10^{18}}\right)^{3/2}$$

for aluminum with $T_e \geq 1 \text{ keV}$ (Terry and Guillory, Ref. 1 p. 5 and plasma radiation transport computations done by Duston (1980)).

The classical heat flux, which is dominated by the Hall flux term $\hat{B} \times \nabla_{\perp} T_e$ since v_e/ω_{ce} is small except very near the axis, would give a cooling rate

$$\dot{T}(\text{keV/ns}) \sim - 3.5 \times 10^{-2} \frac{r_a}{r_T} \left(\frac{A}{26}\right)^{1/2} \left(\frac{10}{z}\right)^{3/2} \left(\frac{10^{18}}{n_i}\right) \left(\frac{1 \text{ mm}^2}{\pi r_a^2}\right) T_{\text{keV}}^{3/2} \quad (29)$$

where r_T is the radial temperature scaleheight.

But the modified two-stream instability^{12,13} grows at a rate about half the lower-hybrid frequency

$$\omega_{\text{LH}} = \sqrt{\omega_{ce} \omega_{ci}} \sim 3 \times 10^{11} \left(\frac{26}{A}\right) \left(\frac{z}{10}\right)^2 \left(\frac{n_i}{10^{18}}\right) \left(\frac{r_a}{1 \text{ mm}}\right)^{1/2} T_{\text{keV}}^{1/2} \quad (30)$$

(based on Eq. (21) for I) and thus can easily saturate in less than 1 ns, leading to alteration of the diffusive heat flux as well as being the source of the drift-speed limiting assumed at the outset.

But the alteration of the heat flux, according to the form of anomalous heat conductivity given by Manheimer¹⁴

$$\kappa \sim cT/16 eB \quad (31)$$

is small and gives a contribution

$$\dot{T}(\text{keV/ns}) \sim 10^{-3} \left(\frac{A}{26}\right)^{1/2} \left(\frac{10}{z}\right)^{3/2} \left(\frac{10^{18}}{n_i}\right) \left[\frac{r(\text{mm})}{\pi r_a^2(\text{mm}^2) \ell^2(\text{mm}^2)} \right] T_{\text{keV}}^{-3/2} \quad (32)$$

to the electron cooling in transit across the anomalous low-density regions. (The inverse dependence on n_i comes only from the linear dependence of I , and thus B , on n_i .)

The instability tries to stabilize by bringing a small number of ions up to the sound speed¹⁵ but this is an important energy drain for the electrons only where $T_e \gg T_i$. For the time development of T_i due to this anomalous heating, one may consult Lampe et al.,¹⁶. A fraction $f_i \sim (m_e/m_i)^{1/2}$ of the ions is accelerated to a speed comparable with c_s , i.e., to energies $\frac{3}{2} T_e$. (The directions are isotropized by the magnetic field.) There is thus a loss of ion thermal energy due to the exit of these particles from the low density region, which is only partly compensated by the thermal influx of ions at temperature T_i . The net heat loss flux per cm^2 of area is

$$n_i f_i \left[\left(\frac{1}{4} c_s \right) \left(\frac{3}{2} T_e \right) - \left(\frac{1}{4} v_{Thi} \right) \left(\frac{3}{2} T_i \right) \right] \quad (33)$$

(v_{Thi} is the ion thermal speed); and when the instability is saturated and quasi-steady this energy loss is made up by energy transfer from electrons to ions via unstable waves:

$$\frac{3}{2} n_e \dot{T}_e \pi r_a^2 \ell a = \pi r_a^2 \left(\frac{3}{8} n_i f_i \right) [c_s T_e - v_{Thi} T_i] .$$

This gives rise to an electron cooling rate . .

$$\dot{T}_e \text{ (keV/ns)} \leq .5 \times 10^{-3} \left(\frac{10}{z} \right)^{1/2} \left(\frac{26}{A} \right)^{3/4} \left(\frac{1 \text{ mm}}{\ell_a} \right) T_{\text{keV}}^{3/2} . \quad (34)$$

This rate is small because of the small number of ions involved, relative to the number of electrons. In fact, for nominal parameters all of the electron cooling rates (27) - (34) are small compared with the Ohmic heating rate, and so most of the Ohmic energy gain is delivered to the blobs after transit across the anomalous region.

Power Delivery

Assuming the dense blobs to be thicker than one range for the 15-50 keV electrons accelerated into them, the total net power delivery to them is

$$P \sim \frac{3}{2} (T_e - T_{eo}) N \pi r_a^2 n_e c_s \quad (35)$$

where $T_e - T_{eo}$ is the temperature gain by Ohmic heating, less losses, during transit from blob to blob. If the cooling during transit is negligible and if almost all the voltage drop occurs across the low-density regions, then the power delivered is

$$P(TW) = 0.36 \left(\frac{V}{1MV} \right) \left(\frac{\pi r_a^2}{1 \text{ mm}^2} \right) \left(\frac{z}{10} \right)^{3/2} \left(\frac{26}{A} \right)^{1/2} \left(\frac{n_i}{10^{18}} \right) T_{keV}^{1/2} \quad (36)$$

with n_i , T_{keV} representing either their average values or their initial (unheated) values in the low-density region. If less than the full voltage drop occurs across the anomalous regions, the value of V above is adjusted downward accordingly.

Peak Electron Temperature

In the low-density regions, the electron temperature varies axially, increasing in the direction of electron flow because of collisional and unstable-wave isotropization of the energy gained from the axial electric field. The temperature begins at approximately its value in the adjacent classical bead (a quasi-balance of deposition and radiative loss), increases as the electron traverses the low density region, and reaches its maximum just before deposition in the next "bead" downstream.

Since the heating during transit has the approximate form $\dot{T}_e \propto T_e^{1/2}$ (from Eq. (25), one has for the case of negligible heat conduction and radiation

$$\left. \begin{aligned} c_s(t) &\approx c_s(0) + \dot{c}_s t \\ \dot{z}(t) &= c_s(t) \end{aligned} \right\} \quad (37)$$

So that $z(t) = \dot{c}_s(0)t + \frac{1}{2} \dot{c}_s t^2$ and the final temperature is such that

$$c_s(t_f) = \sqrt{\dot{c}_s^2 + 2 \dot{c}_s l_a} \quad (38)$$

$$\text{i.e. } T_e(l_a) = T_{eo} + \frac{670 \text{ keV}}{N_a} \left[V(\text{MV}) - LI \right] \quad (39)$$

from Eqs. (20) and (25), as an overestimate of the peak temperature. (N_a , the number of anomalous regions, is observed to be typically of the order of 20 to 30, while the inductively corrected voltage $V - LI$ is one or two MV.) The voltage drop along the classical beads has been neglected compared with that over the anomalous regions between beads, and including it reduces the effective voltage appearing in Eq. (39) to that occurring only over the N_a anomalous regions. In this approximation the temperature increases linearly with distance across each acceleration region.

The indication that the peak electron temperature may be tens of keV implies that Bremsstrahlung and inner shell x-rays can be produced, predominantly on the cathode ends of the classical beads if their density is high enough, or throughout the beads if they are only about one range thick for the energetic electrons.

Inductive Effects

The generalized Ohm's law in a classical medium takes the form

$$E = \eta J + k \dot{J} - \frac{v}{c} \times B \quad (40)$$

$$\text{or } V = RI + L\dot{I} + \dot{L}I \quad (41)$$

(k is a constant related to the electron inertia and the geometry, and L is the self-inductance.) Voltages induced by changing the current-carrying radius r_a are of order

$$E(\text{MV/cm}) \sim 2I(\text{MA}) \frac{\dot{r}_a}{r_a} (\text{ns}^{-1}), \quad (42)$$

which becomes of order 1 MV just before the peak compression. The corresponding impedance

$$\dot{L} (\text{Ohms}) \sim 2l(\text{cm}) \frac{\dot{r}_a}{r_a} (\text{ns}^{-1}) \quad (43)$$

has maximum value on the order of 1 Ohm, in series with 1-4 Ohms effective resistance, and so is not a negligible correction except for a few-nanosecond intervals when $\dot{r}_a \approx 0$. In SPLAT code runs, the \dot{L} term is even somewhat larger, at its maximum, than the Ohmic resistance of the classical plasma core. But where the current becomes limited by anomalous regions in series with classical ones, the effective resistance R^* in the equation

$$V = R^*I + L\dot{I} + \dot{L}I \quad (44)$$

is larger (and voltage-dependent, as V); so the \dot{L} term no longer dominates, although it is not strictly negligible except very near peak compression and for the "pause" phase of "pause-and-collapse" compressions. For our simple description we neglect the \dot{L} term, which is acceptable when V/I is much larger than \dot{L} , i.e.,

$$\frac{\dot{r}_a}{r_a} (\text{ns}^{-1}) \ll 1.4 \frac{V(\text{MV})}{\ell(\text{cm})} \left(\frac{A}{26}\right)^{1/2} \left(\frac{10}{z}\right)^{3/2} \left(\frac{10^{18}}{n_i}\right)^{-1/2} T_{\text{keV}}^{-1/2} \left(\frac{1 \text{ mm}^2}{\pi r_a^2}\right) \quad (45)$$

The $L\dot{I}$ term may be governed by nonlinear sausage instability dynamics not yet well understood; when I is given by Eq. (21), I is proportional to $\frac{d}{dt}(n_i \pi r_a^2)$, i.e., the change in particle number in the necked-off region. This subject is to be investigated under 1981 and 1982 funding, and is beyond the scope of available theory at the time of this report.

Justification of Drift-Speed-Limited Current

When the ion and electron temperatures are comparable one does not get appreciable growth of the ion acoustic instability (Kovrizhnykh, 1967;¹⁸ Biskamp and Chodura, 1971,¹⁹), but the modified two-stream instability (Ott et al;¹³ McBride et al,²⁰) grows with linear growth rate

$$\text{Im } \omega(\text{MTS}) \sim \frac{1}{2} \omega_{\text{LH}} = \frac{1}{2} \omega_{\text{pi}} (1 + \omega_{\text{pe}}^2 / \omega_{\text{ce}}^2)^{-1/2} \approx \frac{1}{2} \omega_{\text{ce}} \sqrt{A/Z} \quad (46)$$

where ω_{LH} is the "lower hybrid" frequency, ω_{pe} is the plasma frequency, and ω_{ce} is the electron gyrofrequency. This persists as long as the drift velocity v_d exceeds approximately the sound speed, c_s , and is marginally stable when $v_d \approx c_s$. The nonlinear saturation time, of order $300 \omega_{\text{pe}}^{-1}$, is much shorter than the ℓ/c_s transit time of electrons across the anode-cathode gap, so the waves can grow to saturation within the diode.

Including the electron magnetization more carefully, one also gets an "electron cyclotron drift instability" (Forslund, Morse and Nielsen²¹ with growth rate

$$\text{Im } \omega(\text{ECD}) \sim \omega_{\text{ce}} \frac{v_d}{v_e} \frac{T_e}{2T_i} - \nu_{ei} \quad (47)$$

where v_d is the electron drift speed, v_e is the electron thermal speed, and ν_{ei} the electron collision frequency as before. But for typical parameter values, v_d/v_e should be of order $\sqrt{A/Z}$ so the two linear growth rates are comparable:

$$\text{Im } \omega \sim 2.6 \times 10^{11} \left(\frac{Z}{10} \frac{26}{A} \right)^{1/2} \frac{I(\text{MA})}{r_a(\text{mm})} \quad (48)$$

as long as this exceeds ν_{ei} in Eq. (18).

The radial gradients in magnetic fields can also give rise to a "lower-hybrid drift" instability (Krall and Liewer,¹²) with linear growth rate

$$\text{Im } \omega(\text{LHD}) \sim \omega_{pi} \left[\frac{1}{2B} \frac{dB}{dr} \frac{v_e^2}{\omega_{ce} c_s} \right]^{\frac{1}{2}} (\omega_{ce}/\omega_{pe})$$

$$\sim 7.4 \times 10^{-5} \omega_{ce} \left[\frac{26}{A} \left(\frac{10}{Z} \right)^3 \frac{T_{\text{keV}}}{h_B^2 B(\text{MG})^2} \right]^{1/4}$$

where $h_B = \left(\frac{1}{B} \frac{dB}{dr} \right)^{-1} \sim r_a(\text{cm})$.

Since B is at most $2I/cr_a$, this gives

$$\text{Im } \omega(\text{LHD}) \leq 10^{10} \frac{I_{\text{MA}}^{\frac{1}{2}}}{r_a(\text{mm})} \left[\left(\frac{26}{A} \right) \left(\frac{10}{Z} \right)^3 T_{\text{keV}} \right]^{1/4} \left(\frac{r_a}{h_B} \right)^{1/2} \quad (49)$$

which is generally less than the MTS and ECD instability growth rates.

Because the modified two-stream instability exponentiates in a few picoseconds and saturates in several growth times, it is most likely that the electron drift speed is limited in this way to values near that which stabilizes the instability, namely the sound speed. This is the justification for the anomalous drift-speed-limited current-carrying behavior assumed earlier.

Application to Cylindrical Implosions
and the "SPLAT" Code

From Eqs. (19) and (20), we easily derive a fact of some significance. Before the field has penetrated a cylindrical z-pinch plasma, the radial profile of the E_z electric field of course goes from negligible values at the current penetration front to values of order V/ℓ at large radii. For all radii where

$$E(r) \text{ (MV/cm)} > \left(\frac{.12}{T_{\text{keV}}} \right) \left(\frac{n_i(r)}{10^{20}} \right) \left(\frac{26}{A} \right)^{1/2} \left(\frac{\ell n \Lambda}{10} \right) \left(\frac{z}{10} \right)^{5/2}, \quad (50)$$

the current is drift-speed limited. For temperatures of order $\frac{1}{2}$ keV and above, the critical $E(r)$ value at $r=a$ is much less than $V/\ell \sim 1\text{MV/cm}$ when $n_i(r)$ is small compared with 10^{20} .

But from the voltage rise time $\tau_v \sim 10^{-7}$ sec, we can estimate a classical skin depth in the dense (classical) region:

$$\Delta(\text{cm}) = 29 \sqrt{\tau_v(\text{sec})} T_{\text{keV}}^{-3/4} \left(\frac{\ell n \Lambda}{10} \frac{z}{10} \right)^{1/2}, \quad (51)$$

and this gives a core current,

$$I_1 = \int_0^a 2\pi r \sigma E(a) e^{-(a-r)/\Delta} dr, \text{ i.e.,}$$

$$I_1(\text{MA}) = 0.21 \left(\frac{\tau_v}{10^{-7}} \right)^{1/2} \left(\frac{z}{10} \right)^2 T_{\text{keV}}^{-1/4} \left(\frac{\ell n \Lambda}{10} \right)^{1/2} \left(\frac{26}{A} \right)^{1/2} a(\text{mm}) \frac{n_i(a)}{10^{18}} \quad (52)$$

When the core carries most of the current ($I \approx I_1$), this gives for the density at the critical surface of radius a

$$\frac{n_i}{10^{18}} = 4.8 \left(\frac{10}{\ell n \Lambda} \frac{A}{26} \right)^{1/2} \left(\frac{10}{z} \right)^2 T_{\text{keV}}^{1/4} \left(\frac{10^{-7}}{\tau_v} \right)^{1/2} \frac{I(\text{MA})}{a(\text{mm})} \quad (53)$$

Thus, for a keV aluminum plasma carrying 1 MA current at the skin of a 1 mm^2 area, if the on-axis density drops below about $10^{19} \text{ ions/cm}^3$ anywhere, then the classical "core" tends to disappear there. And since this value (Eq. 53) of n_1 tends to be small compared with 10^{20} cm^{-3} , most of the E field is shielded from the classical region, i.e., $E(a) \ll V/l$, while there is a classical region.

The one-dimensional strongly-coupled plasma implosion code SPLAT (Terry and Guillory,¹) sets (initially) a radius a beyond which the current is drift speed limited at the initial temperature. In the present form of the code, this radius is then followed in a Lagrangian manner, moving with the fluid velocity. In fact, however, as the temperature and current increase, the real "critical surface" at which conduction becomes anomalous moves inward more rapidly than the particles, following the variable density contour of Eq. (53). Thus a larger and increasing fraction of the current, I_2/I , is carried "anomalously." This fraction is thus underestimated by the code. The corona is actually more important than indicated by the code for another reason: its density at the true "critical surface" $r=a$ is larger than presently accounted for and the total ohmic heating should be larger.

Sausage Instability Dynamics

The nonlinear behavior of the axisymmetric sausage instability has been treated only in a few limiting cases. A nonradiating, perfectly conducting incompressible MHD model with uniform density and no heat conduction was treated by Book, Ott and Lampe.¹⁷ In both the long wavelength ($\lambda \gg r$) and short wavelength limits, these assumptions gave tractable equations, which showed a spool-like development of the plasma shape, with thin rapidly expanding disks of enlarged radius and broad, slowly constricting regions of reduced radius. The presence of finite conductivity and axial electric field certainly modifies the dynamics; and even more so, the inclusion of finite compressibility, which is being studied now by Book et al, may greatly alter the conclusions made in the simpler model.

Because of this, we have proposed in our 10/81-10/82 program an extension of the Book et al theory to include finite conductivity and E field, and the construction of a 2-dimensional r-z code for modeling the behavior with radiation, circuit model, etc. coupled into the dynamics.

The equations describing the motion are:

$$\begin{aligned}
 \text{continuity:} \quad & \partial_t \rho + \partial_z (\rho v_z) + \frac{1}{r} \partial_r (\rho r v_r) = 0 \\
 \rho D\vec{v}/Dt = \nabla P: \quad & \rho (\partial_t v_z + v_z \partial_z v_z + v_r \partial_r v_z) = - \partial_z P \\
 & \rho (\partial_t v_r + v_z \partial_z v_r + v_r \partial_r v_r) = - \partial_r P \\
 \text{state:} \quad & P = \gamma T \rho / m_i + B^2 / 8\pi + K B^2 / r \quad B^2 = B^2(r, z) \\
 \nabla \times B: \quad & \frac{1}{r} \partial_r (r B) = \frac{4\pi}{c} J_z; \quad - \partial_z B = \frac{4\pi}{c} J_r \\
 \nabla \times E: \quad & \partial_z E_r - \partial_r E_z = - \frac{1}{c} \partial_t B \\
 \nabla \cdot J = 0: \quad & \frac{1}{r} \partial_r (r J_r) + \partial_z J_z = 0
 \end{aligned} \tag{54}$$

Ohm's Law:

$$J_z = \text{Min} \left\{ \frac{0}{m} z k_J T^{\frac{1}{2}}, \left\{ k_J T^{3/2} \left(E_z + \frac{v_r B}{c} \right) \left(1 + \frac{k_O^2 T^3 B^2}{k_B^2 \rho^2} \right)^{-1} \right. \right.$$

$$\left. \left. + k_B \rho T^{-3/2} \left(\frac{E_r}{B} - \frac{v_z}{c} \right) \left(1 + \frac{k_B^2 \rho^2}{k_O^2 T^3 B^2} \right)^{-1} \right\} \right\}$$

$$J_r = \text{Min} \left\{ \frac{0}{m} z k_J T^{\frac{1}{2}}, \left\{ k_O T^{3/2} \left(E_r - \frac{v_z B}{c} \right) \left(1 + \frac{k_O^2 T^3 B^2}{k_B^2 \rho^2} \right)^{-1} \right. \right.$$

$$\left. \left. + k_B \rho T^{-3/2} \left(\frac{E_z}{B} + \frac{v_r}{c} \right) \left(1 + \frac{k_B^2 \rho^2}{k_O^2 T^3 B^2} \right)^{-1} \right\} \right\}$$

Heat balance: T specified as function of discharge voltage and ρ , in simplest model, or governed by time dependent heating and cooling rates, in more complex model.

The radial component of J cannot be neglected because then $\partial_z B = 0$ does not allow the instability. The constants k_O in the unmagnetized conductivity and k_B in the Hall conductivity can be found in the standard textbooks; the constant k_J (see Eq. (21)) gives the drift-speed limited current. The constant K provides the magnetic hoop stress due to B-line curvature. The mass density is denoted by ρ , electron (and ion) temperature by T , and fluid velocity by (v_r, v_z) . All field and fluid quantities are functions of r and z . Imposing self-similar convex profiles of ρ with radius (e.g., Bennett profiles) and periodicity in z , with only the on-axis density and Bennett radius varying in z , may allow certain artificial but useful simplifications. Making the ideal-MHD assumption is not admissible here, as it allows only surface currents and cannot predict the density drop in the necked-off regions. The fluid model described may break down when these regions produce non-stagnated electron flows.

CHAPTER V. CURRENT PROBLEMS

A. Improved numerical methods

As pointed out above, there are several advantages to the use of the generalized Hertz vector $Z(r,t)$ as a potential for the waveguide fields driving an imploding plasma. The price of this smooth generality is that all the observable fields are two derivatives removed from the potential. Hence we require very accurate numerical differentiation methods for the estimation of E_z , B_θ from any discrete representation, i.e. $Z(x_j, \tau_i)$ and $\dot{Z}(x_j, \tau_i)$. Moreover, as the plasma load absorbs and reflects the incoming electromagnetic wave, the rapid decay of $E_z(x, \tau)$ within the plasma demands the resolution of the derivatives of $Z(x, \tau)$ over a very small spatial scale. Adding to the challenge, one must assess third and fourth order derivatives in calculating the source terms in the wave equation for $Z(x, \tau)$.

The usual finite difference methods, based on polynomial interpolation, tend to produce rather noisy estimates of higher derivatives unless the spatial mesh is quite dense. Recent work by Talmi and Gilat²², however, offers a solution to this problem by using a so-called smooth interpolation. In classical analysis the error functional, measuring the global deviation of an interpolant from the original function, is usually based on the Hilbert norm. Minimizing error with respect to this norm does not constrain the derivatives of the interpolant and often leads to rather bizarre behavior. The generalization due to Talmi and Gilat which leads to a smooth interpolant is the invention of a norm functional which involves all higher derivatives as well as function amplitudes in computing an error measure.

This new method has been implemented recently and has generated encouraging results interpolating simple test functions. Function values can be represented to 7 significant figures, and second derivatives to 4 significant figures. This sort of performance is not quite sufficient for use with the Hertz potential, but it is quite adequate for the representations of CRE radiation and ionization dynamics required in section B, below. The investigation at present is focused on the optimal tradeoff between the number of sample points and the correlation width which determines the effective coupling domain among points on the mesh. There is every reason to believe that the satisfactory representation of third and higher derivatives is within the capabilities of this new method.

B. Alternative thermodynamic variables for ionization dynamics

In hydrodynamic calculations requiring ionization dynamics a central problem is the branching ratio, for external energy input to the fluid, between electron heating and further ionization. As each new atomic shell structure is opened to ionization (because the electron thermal energies and radiation intensity have achieved an appropriate threshold) this branching ratio changes radically with a large fraction of the input energy going to further ionization rather than electron heating. On the other hand, any attempt to calculate $\frac{DT}{Dt}$ and advance the plasma state with \mathcal{Z} and ϵ_I (the chemical potential) held fixed, only to then require a fresh value of ϵ_I and \mathcal{Z} at some new temperature T_e^* , will lead to serious inaccuracy and perhaps numerical instabilities if the ionization energy is recovered from T_e^* . This is why the branching ratios $\partial_{T_e} \mathcal{Z}$, $\partial_{T_e} \epsilon_I$ and (to a lesser extent) $\partial_{n_I} \mathcal{Z}$, $\partial_{n_I} \epsilon_I$ are so important.

The calculation of these ratios from first principles within the CRE framework is not an easy task, but their estimation by means of the smooth interpolation discussed above is both simple and accurate. The CRE model implies an effective equation of state $\epsilon_I(T_e, n_I)$ and $\mathcal{Z}(T_e, n_I)$ which can be used to simplify the simultaneous calculations of electron heating and ionization. Instead of using T_e one may define a new energy variable

$$\frac{3}{2} \theta_e = \frac{3}{2} \mathcal{Z} T_e + \epsilon_I(T_e) \text{ and } T_e = T_e(\theta_e),$$

its inverse function. The appropriate hydrodynamic equations now advance θ_e and T_I using the usual heat sources and fluxes; viz.

$$\begin{aligned} \frac{3}{2} \frac{D}{Dt} \theta_e &= \frac{DT}{Dt} \cdot \left[\frac{3}{2} T_e \frac{\partial \mathcal{Z}}{\partial T_e} + \frac{3}{2} \mathcal{Z} + \frac{\partial \epsilon_I}{\partial T_e} \right] + \frac{Dn_I}{Dt} \cdot \left[\frac{3}{2} T_e \frac{\partial \mathcal{Z}}{\partial n_I} + \frac{\partial \epsilon_I}{\partial n_I} \right] \\ \frac{D}{Dt} T_I &= - \frac{2}{3} T_I (\nabla \cdot \underline{V}) - \underline{\nabla} \cdot \underline{q} - \pi : \underline{\nabla} \underline{V} + \frac{3m_e}{m_i} \mathcal{Z} (T_e(\theta_e) - T_I) \cdot \tau_{Ie} \end{aligned} \quad (55)$$

where the partial derivatives and functions $\theta_e(T_e)$ arising from the CRE model are represented by a smooth interpolant.

Present efforts in achieving this reformulation are directed toward finding the best temperature and density domain grid and optimal interpolation parameters. In addition, the restructuring of present hydrodynamic codes to accept these new variables is underway.

REFERENCES

1. R. E. Terry and J. Guillory JAYCOR Report No. TPD200-80-001-DFR, July 1980.
2. D. Duston and J. Davis, Phys. Rev. A 21, May 1980.
3. D. Duston, private communication.
4. J. Apruzese, private communication.
5. R. E. Terry and J. Guillory JAYCOR Report No. TPD-200-80-001-DFR, pp. 67-70, July 1980.
6. M. Gersten, private communication.
7. J. Katzenstein, "Optimum Coupling of Imploding Loads to Pulse Generators.", Maxwell Laboratory Report.
8. R. E. Terry and J. Guillory, JAYCOR Rpt. No. TPD200-80-012, 10/80, pp. 13-15.
9. J. A. Stratton, Electromagnetic Theory, McGraw Hill, New York, 1941 1st Ed., p. 28.
10. W. R. Smythe, Static and Dynamic Electricity, McGraw Hill, New York 1968, 3rd Ed., p. 416.
11. Shyke Goldstein, in H. W. Bloomberg, et al., "Energy Coupling Mechanisms in Multiple Wire Array Configurations." Science Applications, Inc. Report #SAI-102-72-004, (1979).
12. N. A. Krall and P. C. Liewer, "Low-Frequency Instabilities in Magnetic Pulses," Phys. Rev. A4, 2094 (1971).
13. E. Ott, J. B. McBride, J. H. Orens, and J. P. Boris, "Turbulent Heating in Computer Simulations of the Modified Plasma Two-Stream Instability," Phys. Rev. Lett. 28, 88 (1972).
14. W. M. Manheimer, "Anomalous Transport from Plasma Waves," Journal de Physique, 40, C7-269 (1979) Suppl.;
15. G. E. Vekshtein, D. D. Ryutov and R. Z. Sagdeev, "Asymptotic Solution of the Problem of the Anomalous Resistance of a Collisionless Plasma." Sov. Phys. JETP 33, 1152 (1971).

16. M. Lampe, W. M. Manheimer, J. B. McBride, J. H. Orens, R. Shanny and R. N. Sudan, "Nonlinear Development of the Beam-Cyclotron Instability," Phys. Rev. Lett. 26, 1221 (1971).
17. D. L. Book, E. Ott, and M. Lampe, "Nonlinear Evolution of the Sausage Instability" Phys. Fluids 19, 1982 (1976).
18. L. M. Kovrizhnykh, "Nonlinear Theory of Current Instability in a Non-isothermal Plasma." Sov. Phys. JETP 24, 1210 (1967).
19. D. Biskamp and R. Chodura, "Computer Simulation of Anomalous Resistance." Phys. Rev. Lett. 27, 1553 (1971).
20. J. McBride, E. Ott, J. Boris, and J. Orens, "Theory and Simulation of Turbulent Heating by the Modified Two-Stream Instability." Phys. Fluids 15, 2367 (1972).
21. D. W. Forslund, R. L. Morse, and C. W. Nielson, "Nonlinear Electron-Cyclotron Drift Instability and Turbulence" Phys. Rev. Lett. 27, 1424 (1971).
22. A. Talmi and G. Gilat, Journal of Computational Physics 23, 93, (1977).
23. S. I. Braginskii in Reviews of Plasma Physics, ed. M. A. Leontovich (Consultants Bureau, N.Y., 1965), p. 249 ff.
24. P. J. Davis and I. Polonsky, Handbook of Mathematical Functions, NBS AMS-55 (ed. M. Abramovitz and I. A. Stegun), USGPO (1964).
25. A. H. Stroud, Approximate Calculation of Multiple Integrals, Prentice Hall, Englewood Cliff, NJ (1971), (pp. 267-289).

APPENDIX A

FIELD REPRESENTATIONS

The procedure for choosing \underline{Z} can be formalized easily and points out the role of a Hertz vector potential in the conventional scheme of electrodynamics.

Field Representation Theorem:

- a) Given potentials \underline{A} , ϕ satisfying the Lorentz gauge condition, the choice $\underline{Z} \stackrel{d}{=} \int dt \int \underline{A}(\underline{x}, t_1)$ implies that $\phi \equiv -\underline{\nabla} \cdot \underline{Z}$ and (obviously) that $\underline{A} \equiv c^{-1} \partial_t \underline{Z}$.
- b) Given the vector field \underline{Z} , the choice $\underline{A} \stackrel{d}{=} c^{-1} \partial_t \underline{Z}$ and $\phi \stackrel{d}{=} -\underline{\nabla} \cdot \underline{Z}$ implies that \underline{A} , ϕ satisfy a Lorentz gauge condition. Moreover, the transformation $\underline{Z} \rightarrow \underline{Z}' = \underline{Z} + \underline{\nabla} \psi$ with ψ any solution of $\square^2 \psi = 0$ is the generator of all restricted gauge transformations (within the Lorentz gauge) which leave the observable fields \underline{E} , \underline{B} invariant.

This result is readily established, as summarized below. With \underline{A} , ϕ in the Lorentz gauge and \underline{Z} defined through \underline{A} , the gauge condition on \underline{A} , ϕ implies that $\phi = -\underline{\nabla} \cdot \underline{Z}$ and, of course, $\underline{A} \equiv c^{-1} \partial_t \underline{Z}$. On the other hand, given \underline{Z} and \underline{A} , ϕ defined through \underline{Z} , the Lorentz gauge condition is an immediate consequence, and simple substitution verifies that \underline{Z}' as given preserves the gauge and leaves \underline{E} , \underline{B} invariant. Of course, if \underline{A} , ϕ are to be represented on all spacetime by one field, \underline{Z} , it must be shown that only one non-trivial propagation equation is needed for evolving this new field \underline{Z} . This is in fact the case.

Uniqueness Theorem for $\underline{Z}(\underline{x}, t)$: Let initial fields \underline{E}^0 and \underline{B}^0 be specified on all space at some time t_0 , together with a source field \underline{T} (equivalently ρ and \underline{J}) on a domain $(\underline{x}, t \geq t_0)$ and boundary conditions of the form $c_1 \underline{E}(\underline{x}, t) + c_2 \underline{B}(\underline{x}, t)$ on any surfaces of discontinuity that are present. The generalized Hertz vector $\underline{Z}(\underline{x}, t)$, as a solution of $\underline{\nabla}(\underline{\nabla} \cdot \underline{Z}) - \underline{\nabla} \times \underline{\nabla} \times \underline{Z} - c^{-2} \partial_t^2 \underline{Z} = -4\pi \underline{T}$, is then specified

uniquely (to within a trivial restricted gauge transformation) and stably on $(\underline{x}, t \geq t_0)$.

The proof is somewhat lengthy but, in summary, decompose \underline{Z} and \underline{T} into solenoidal $(\underline{Z}^t, \underline{T}^t)$ and lamellar $(\underline{Z}^l, \underline{T}^l)$ parts. For the solenoidal fields, the initial specification of $\underline{E}_0^t, \underline{B}_0$, and $\underline{J}^t (\equiv \partial_t \underline{T}^t)$ is equivalent to an initial specification of $\underline{Z}^t|_{t_0}$ and $\partial_t \underline{Z}^t|_{t_0}$. For the lamellar fields the initial specification of $\underline{E}_0^l (\equiv -4\pi \underline{T}_0^l)$ and \underline{J}^l is equivalent to an initial specification of $\underline{Z}^l|_{t_0}$ and $\partial_t \underline{Z}^l|_{t_0}$. The homogeneous solution for \underline{Z} must then be selected to produce the specified boundary conditions. The specification of $\underline{Z}|_{t_0}$ and $\partial_t \underline{Z}|_{t_0}$ required by the initial conditions thus constitutes Cauchy open surface boundary conditions and a unique, stable solution exists for the \underline{Z} wave equation. The ambiguity in \underline{Z} with respect to the restricted gauge transformations can be erased by simply setting to zero all trivial constants of integration in the inverse mapping $\{\underline{E}^0, \underline{B}^0\} \rightarrow \{\underline{Z}|_{t_0}, \partial_t \underline{Z}|_{t_0}\}$.

APPENDIX B

HERTZ VECTOR POTENTIAL FOR THE PLASMA LOADED WAVEGUIDE

Using the Green's function one can decompose any vector field $\underline{b}(\underline{x}, t)$ into its solenoidal ($\underline{\nabla} \cdot \underline{b} = 0$) and lamellar ($\underline{\nabla} \times \underline{b} = 0$) components; these projection operators can be represented

$$\underline{1} \underline{b} \equiv (4\pi)^{-1} \underline{\nabla} \times \int d\tilde{\underline{x}} G(\underline{x}, \tilde{\underline{x}}) \underline{\nabla} \times \underline{b}(\tilde{\underline{x}}, t)$$

$$|| \underline{b} \equiv - (4\pi)^{-1} \underline{\nabla} \int d\tilde{\underline{x}} G(\underline{x}, \tilde{\underline{x}}) \underline{\nabla} \cdot \underline{b}(\tilde{\underline{x}}, t)$$

and can be used to invert the differential equations $\underline{\nabla} \times \underline{b} = \underline{S}_\perp$ and $\underline{\nabla} \cdot \underline{b} = S$ for the field \underline{b} . For the case of spacetime dependent conductivity, such operations are central to the construction of the proper Hertz vector, because the vector equation for $\underline{A}(\underline{Z})$ one must solve in order to obtain a homogeneous equation for (4b) is

$$\underline{\nabla} \times \underline{\nabla} \times \underline{A}(\underline{Z}) = c^{-1} (\partial_t + 4\pi \tilde{\sigma}) \underline{\nabla} \times \underline{\nabla} \times \underline{Z} + \frac{4\pi \tilde{\sigma}}{2} \underline{\nabla} \times \underline{\nabla} \times \underline{A}(\underline{Z}). \quad (B1)$$

In order to solve (B1) one may define two vector functionals in terms of the Greens function $G(\underline{x}, \tilde{\underline{x}}) = G(\underline{x} - \tilde{\underline{x}})$ and the projection operators $\underline{1}$, $||$. A lamellar functional of any scalar is obtained from $||$, viz.

$$\underline{g}^l(s) \equiv - \underline{\nabla} \int \frac{d\tilde{\underline{x}}}{4\pi} G(\underline{x} - \tilde{\underline{x}}) s(\tilde{\underline{x}}, t)$$

is a curlless field solving $\underline{\nabla} \cdot \underline{g}^l = s$. A solenoidal functional of any vector is obtained through $\underline{1}$, i.e.,

$$\underline{g}^t(\underline{\lambda}^t) \equiv \int \frac{d\tilde{\underline{x}}}{4\pi} G(\underline{x} - \tilde{\underline{x}}) \underline{1} \underline{\lambda}(\tilde{\underline{x}}, t)$$

is a divergenceless field solving $\underline{\nabla} \times \underline{\nabla} \times \underline{g}^t = \underline{\lambda}^t$. These functionals can invert (B1) whenever the RHS is a truly solenoidal field. The orthogonality conditions (11 a,b,c) and the condition that $\underline{\nabla} \sigma \cdot \underline{\nabla} \underline{x} \underline{\nabla} \underline{x} \underline{Z} = 0$ are sufficient to insure a solenoidal RHS for (B1); one must find the appropriate s and $\underline{\lambda}$.

For s one possibility is the commutator

$$[\underline{\nabla} \cdot \underline{\tilde{\sigma}} \underline{Z}, \underline{\tilde{\sigma}} \underline{\nabla} \cdot \underline{Z}] = \underline{Z} \cdot \underline{\nabla} \underline{\tilde{\sigma}} \quad , \quad (B2a)$$

and for $\underline{\lambda}$, the commutator

$$[\underline{\nabla} \times \underline{\nabla} \times \underline{\tilde{\sigma}} \underline{Z}, \underline{\tilde{\sigma}} \underline{\nabla} \times \underline{\nabla} \times \underline{Z}] = (\underline{\nabla} \underline{\tilde{\sigma}} \times \underline{\nabla} \times \underline{Z}) + \underline{\nabla} \times (\underline{\nabla} \underline{\tilde{\sigma}} \times \underline{Z}) \quad . \quad (B2b)$$

Taking the limit $c^{-1} \underline{V}(\underline{x}, t) \rightarrow 0$ in (B1) one finds that the field functional

$$\begin{aligned} \underline{A}^{(o)}(\underline{Z}) = & c^{-1}(\partial_t + 4\pi \underline{\tilde{\sigma}}) \underline{Z} - \underline{g}^{\ell} \left\{ \frac{4\pi}{c} \underline{\nabla} \underline{\tilde{\sigma}} \cdot \underline{Z} \right\} - \underline{g}^t \left\{ \frac{4\pi}{c} (\underline{\nabla} \underline{\tilde{\sigma}} \times \underline{\nabla} \times \underline{Z}) + \right. \\ & \left. \frac{4\pi}{c} (\underline{\nabla} \times \underline{\nabla} \underline{\tilde{\sigma}} \times \underline{Z}) \right\} \end{aligned} \quad (B3)$$

in a solution of (B1) provided that the commutator (B2b) is indeed a solenoidal field, a property insured if and only if $\underline{\nabla} \underline{\tilde{\sigma}} \cdot \underline{\nabla} \times \underline{\nabla} \times \underline{Z} \equiv \underline{\nabla} \underline{\tilde{\sigma}} \cdot \underline{E}^t = 0$ as assumed. The result for $\underline{A}^{(o)}(\underline{Z})$ gives

$$\begin{aligned} \underline{\nabla} \cdot \underline{A}^{(o)} &= c^{-1}(\partial_t + 4\pi \underline{\tilde{\sigma}}) \underline{\nabla} \cdot \underline{Z} \\ \underline{\nabla} \times \underline{\nabla} \times \underline{A}^{(o)} &= c^{-1}(\partial_t + 4\pi \underline{\tilde{\sigma}}) \underline{\nabla} \times \underline{\nabla} \times \underline{Z} \end{aligned}$$

for all functions $\underline{\tilde{\sigma}}(\underline{x}, t, \underline{V}^2(\underline{x}, t))$ because the functionals \underline{g}^{ℓ} and \underline{g}^t have been chosen so as to cancel all $\underline{\nabla} \underline{\tilde{\sigma}}$ dependent terms. Noting that $\underline{\nabla} \cdot \underline{A}^{(o)}$ has now provided the possibility of a proper gauge transformation when $\underline{\nabla} \cdot \underline{Z} \stackrel{d}{=} \phi$, the remainder of (B1) must be solved with a \underline{g}^t functional if this result is to be preserved easily. Assume that $\underline{A}(\underline{Z}) = \underline{A}^{(o)}(\underline{Z}) + \underline{g}^t$ and the equation determining \underline{g}^t is, from (B1),

$$\underline{\nabla} \times \underline{\nabla} \times \underline{g}^t = \frac{4\pi \underline{\tilde{\sigma}}}{c^2} \underline{\nabla} \times \underline{\nabla} \times [\underline{A}^{(o)}(\underline{Z}) + \underline{g}^t] \quad .$$

The complete solution is obtained by iterating for the remaining unknown (solenoidal) component of $\underline{A}(\underline{Z})$, i.e., \underline{g}^t . This results in a spatially ordered exponential operator, i.e., $|\underline{x}_1| > |\underline{x}_2| > |\underline{x}_3| \dots$ in successive integrations (convolutions) with $G(\underline{x}, \underline{x})$. The complete expansion of $\underline{A}(\underline{Z})$ is then compactly expressed as

$$\underline{A}(\underline{Z}) = \exp + \left[\int \frac{d\underline{x}}{4\pi} G(\underline{x}, \underline{x}) \left\{ \frac{\tilde{\sigma}}{c}(\underline{x}, t) \frac{\underline{V}}{c}(\underline{x}, t) \times \underline{\nabla} \times \right\} \right] \underline{A}^{(0)}(\underline{Z}) \quad (B4)$$

to all orders in $c^{-1} \underline{V}(\underline{x}, t)$. With this solution available one finds that \underline{Z} is propagated according to

$$\underline{\nabla}(\underline{\nabla} \cdot \underline{Z}) - \underline{\nabla} \times \underline{\nabla} \times \underline{Z} - c^{-1} \partial_t \underline{A}(\underline{Z}) = 0, \quad (B5)$$

which properly subsumes the relation (4a) when one identifies $\phi = -\underline{\nabla} \cdot \underline{Z}$ and notes that $\underline{\nabla} \cdot \underline{A}(\underline{Z}) = \underline{\nabla} \cdot \underline{A}^{(0)}(\underline{Z})$. In particular, (B3) and (B4) imply the novel gauge choice

$$\underline{\nabla} \cdot \underline{A} + c^{-1} \left[\partial_t + 4\pi \tilde{\sigma}(\underline{x}, t, \underline{V}(\underline{x}, t)) \right] \phi(\underline{x}, t) = 0, \quad (B6)$$

and the scalar potential evolution (implied by (B5) or by the substitutions for $\underline{A}(\underline{Z})$, $\phi(\underline{Z})$ in (4a)) is governed by

$$\nabla^2 \phi - 4\pi c^{-1} \partial_t (\tilde{\sigma}(\underline{x}, t, \underline{V}(\underline{x}, t)) \phi(\underline{x}, t)) - c^{-2} \partial_t^2 \phi = 0. \quad (B7)$$

From these results it can be seen that the self-consistent retention of the assumed orthogonality relations (11a, b, c) is possible when $\tilde{\sigma} = \tilde{\sigma}(r, t) \gamma(|\underline{V}_T(r, t)|)$, $\underline{V} = \underline{V}_T(r, t)$, and $\phi = -\underline{\nabla} \cdot \underline{Z} = \nabla \cdot \hat{z} \zeta^k(z, t) \equiv 0$. This is because the pure radial variation of \underline{V} , $\tilde{\sigma}$ allows the wave fields to interact coherently with the load over all axial positions and because, cf. (B7), the radial variation in $\tilde{\sigma}$ is incompatible with a pure axial variation in ϕ if $\tilde{\sigma}$ is non-zero. The perfectly conducting boundary condition on the guide surface forces the scalar potential to be attenuated everywhere once a nonzero conductivity exists anywhere in the radial direction. This coupling means that only the transverse waves (TEM modes) arising through $\zeta^k(r, t)$ can exist in the waveguide formed by perfect conductors. These transverse fields are completely adequate for the maintenance of the proper orthogonality, however, since $\underline{\nabla} \tilde{\sigma} \cdot \underline{\nabla} \times \underline{\nabla} \times \underline{A}(\underline{Z}) \equiv 0$, $\underline{\nabla} \sigma \cdot \underline{\nabla} \times \underline{\nabla} \times \underline{Z} \equiv 0$, $\underline{\nabla} \cdot \underline{V}_T \equiv 0$, and $\underline{\nabla} \sigma \times \underline{V}_T \equiv 0$ are valid forever if valid initially.

The implication of (B3 - B7) and the self-consistent retention of the orthogonality conditions is that a proper Hertz vector has been chosen. Again the reduction to a single propagation equation (B5) for \underline{Z} has simplified the problem, considerably extending the program of reduction available in the simpler case. In contrast to that simpler case of arbitrary but specified ρ , \underline{J} , the present technique has absorbed all reflected wave components in the non-local convolutions involving $G(\underline{x}, \underline{\tilde{x}})$ and has eliminated the need for an explicit source term to produce them. In the event that $\underline{\nabla} \sigma \cdot \underline{E}$ cannot be assumed to vanish, e.g. in the case of resistive guide planes, this approach can probably be made to work but the problem is more difficult and remains under study.

Specializing completely to the plane parallel perfectly-conducting diode geometry and using circular cylindrical coordinates, one may integrate out the trivial azimuthal coordinate in $G(\underline{x}, \underline{\tilde{x}})$, expand the operators in (B5) through first order in $c^{-1} V_r(r, t)$ and $\underline{\nabla} \ln \tilde{\sigma}$, and thus obtain the non-local (radial) propagation equation for $\underline{Z}(r, t) = \hat{z} \zeta^t(r, t)$. Suppressing the vector notation for Z and noting the space-time dependence of $\tilde{\sigma}$, this relation becomes

$$\begin{aligned} c^{-2} \partial_t^2 Z - r^{-1} \partial_r r \partial_r Z + c^{-1} \partial_t \left\{ \frac{4\pi \tilde{\sigma}}{c} Z + 4\pi c^{-1} \int_r^\infty dr_1 Z(r_1, t) \partial_{r_1} \tilde{\sigma}(r_1, t) \right. \\ \left. - 4\pi c^{-1} \ln r \int_0^r dr_1 r_1 \left[(\partial_{r_1} Z) (\partial_{r_1} \tilde{\sigma}) - \frac{\tilde{\sigma}}{c} \frac{V_r}{c} \left[c^{-1} \partial_t + \frac{4\pi \tilde{\sigma}}{c} \right] \partial_{r_1} Z \right] \right. \\ \left. - 4\pi c^{-1} \int_r^\infty dr_1 r_1 \ln r_1 \left[(\partial_{r_1} Z) (\partial_{r_1} \tilde{\sigma}) - \frac{\tilde{\sigma}}{c} \frac{V_r}{c} \left[c^{-1} \partial_t + \frac{4\pi \tilde{\sigma}}{c} \right] \partial_{r_1} Z \right] \right\} = 0. \end{aligned} \quad (B8)$$

The observable fields E_z , B_θ are then obtained from $Z(r, t)$, the solution of (B8), as

$$E_z = -r^{-1} \partial_r r \partial_r Z(r, t) \quad (B9a)$$

$$B_{\theta} = -\partial_r \left[c^{-1} \partial_t Z + \frac{4\pi\tilde{\sigma}}{c} Z + 4\pi c^{-1} \int_r^{\infty} dr_1 Z(r_1, t) \partial_r \tilde{\sigma}(r_1, t) \right.$$

(B9b)

$$\left. - \frac{4\pi}{c} \ln r \int_0^r dr_1 r_1 \left[(\partial_{r_1} Z) (\partial_{r_1} \tilde{\sigma}) - \frac{\tilde{\sigma}}{c} \frac{V_r}{c} \left[c^{-1} \partial_t + \frac{4\pi\tilde{\sigma}}{c} \right] \partial_{r_1} Z \right] \right.$$

$$\left. - \frac{4\pi}{c} \int_r^{\infty} dr_1 r_1 \ln r_1 \left[(\partial_{r_1} Z) (\partial_{r_1} \tilde{\sigma}) - \frac{\tilde{\sigma}}{c} \frac{V_r}{c} \left[c^{-1} \partial_t + \frac{4\pi\tilde{\sigma}}{c} \right] \partial_{r_1} Z \right] \right.$$

and the field $(\tilde{\sigma} \mathbf{E}'_z \times \mathbf{B}_{\theta})$ then provides the self-consistent coupling to the fluid conductor required to calculate $V_r(r, t)$.

APPENDIX C

COUPLING OF FLUID AND FIELD EQUATIONS

If (B8, and B9) are to be coupled to an annular fluid plasma load, represented by scalar fluid fields $n_I(r,t)$, $\tilde{\sigma}(r,t)$, $T_e(r,t)$, $T_I(r,t)$, and the convection vector field $V_r(r,t)$, then one must examine the detailed constitutive relation $J' = \tilde{\sigma}E'$ appropriate to the plasma and verify that all plasma behavior is compatible with the orthogonality constraints used in the electrodynamics. Insofar as strict weakly coupled plasma theory exhibits a linear but anisotropic Ohm's law, the simple constitutive relation used in developing the Hertz vector is not rigorously correct. However, it is easily seen that to a very good approximation the conductivity tensor is "diagonal on a slow timescale", i.e., the radial E , J , can relax on the time-scale characteristic of the electron e/m to cancel the radial currents and to produce a quasi-static ambipolar space charge and a simple quasi-static line-image-charge radial electric field vector. In the axial direction the simple (spacetime dependent) $\tilde{\sigma}(r,t)$ is also appropriate only on a slow time scale as the relative electron flow velocity field relaxes to a steady state for fixed E'_z .

Following Braginskii²³ one may derive two independent relations from the kinetic theory moment equation connecting $\partial_t J \equiv \int d^3v \sum_i q_i \bar{n}_i v \partial_t f_i(\underline{x}, \underline{v}, t)$ to the impressed fields E , B within the plasma. Here "i" is a species index over the appropriate set of one-body LTE distribution functions for the plasma. In the limit that radial plasma conduction currents are divergenceless (quasi-static ρ ambipolar), all plasma gradients are radial, and all neutral convection is radially directed and axially independent, these relations (with $i=e, I$) for the axial and radial currents become, respectively,

$$(1-\chi) \dot{U}_z = -\frac{e}{m_e} \left(1 + \frac{2m_e}{m_I}\right) \left\{ E'_z + \tilde{\beta}_x e^{-1} \partial_r T_e + \frac{m_e \tilde{\alpha}_\perp}{e\tau_e} U_z \right\} \quad (C1a)$$

$$\begin{aligned} (V_r \dot{\chi} + \chi \dot{V}_r) = \frac{e}{m_e} \left\{ \left(1 + \frac{2m_e}{m_I}\right) E_r + c^{-1} U_z \times B_\theta + \partial_r P_e - \frac{2m_e}{m_I} \partial_r P_I \right. \\ \left. - \left(1 + \frac{2m_e}{m_I}\right) \frac{m_e}{e\tau_e} \tilde{\alpha}_x U_z + \left(1 + \frac{2m_e}{m_I}\right) \tilde{\beta}_\perp e^{-1} \partial_r T_e \right\} \end{aligned} \quad (C1b)$$

$$\text{where } \tau_e = \frac{3}{4} \left(\frac{m_e}{2\pi}\right)^{1/2} \frac{T_e^{3/2}}{\Lambda e^4 Z^2 n_I},$$

$$U_z = -J_z (e n_e)^{-1},$$

$$\chi \equiv \rho^{\text{amb}} (e g n_I)^{-1}$$

$$\frac{n_e}{2n_I} = 1 - \chi,$$

and $\tilde{\alpha}$, $\tilde{\beta}$ are dimensionless functions of $\Omega_e \tau_e$ as given by Braginskii, with X, \perp , denoting particular tensor components. As shown (C1a) represents an equation of motion for an "average electron", driven by E'_z and $\partial_r T_e$ and subjected to a drag $(m_e \tilde{\alpha}_\perp / e\tau_e) U_z$ proportional to the velocity achieved. On a timescale characteristic of the electron inertia this "pseudo-particle" will achieve a terminal velocity determined by the condition $\dot{U}_z \sim 0$.

Similarly, (C1b) represents a force balance for an "average electron" which is responding to the space charge field E_r created by pressure and temperature gradients and U_z . Again, on an electron inertia timescale the space charge field self-consistently relaxes to a state of equilibrium stress in response to U_z , $\partial_r P_e$, $\partial_r P_I$, $\partial_r T_e$, i.e., $\dot{\chi} \sim 0$.

Since the inertia of the electron fluid is quite small relative to that of the ion component, a fully self-consistent treatment of the evolution in $\underline{V}_r(r,t)$ which is fundamentally an ion fluid response, and $\underline{Z}(r,t)$ (the electromagnetic field incident on the plasma), is possible in the approximation that both U_z and χ relax rapidly to equilibrium values as \underline{V}_r , \underline{Z} evolve. For the axial conduction current component, this approximation implies the same constitutive relation used in developing \underline{Z} in the first place, with a quasi-static B_θ arising from the thermoelectric field $-\tilde{\beta}_x n_e^{-1} \partial_r T_e$ added to the waveguide field, of course. Substituting for J_z in C1a with $\dot{U}_z \rightarrow 0$, one has

$$J_L = \tilde{\sigma} E' + J_{the} \quad (C2)$$

with

$$\tilde{\sigma}(r,t) \equiv \gamma \left\{ \frac{e^2}{m_e} \mathcal{J} n_I(r,t) \tau_e(r,t) / \tilde{\alpha}_L (\Omega_e(r,t), \tau_e(r,t)) \right\},$$

and

$$J_{the} \equiv \frac{d}{dt} \tilde{\sigma}(r,t) \tilde{\beta}_x (\Omega_e \tau_e) e^{-1} \partial_r T_e.$$

The conductivity $\tilde{\sigma}(r,t)$ defines the plasma location through its density-dependent terms, if the complete expression for τ_e is substituted;

$$\tilde{\sigma}(r,t) = \frac{3}{4} \gamma \left\{ (2\pi m_e)^{-1/2} T_e^{3/2}(r,t) / e^2 \mathcal{J} \tilde{\alpha}_L (\Omega_e \tau_e) \Lambda(n_e(r,t), T_e(r,t)) \right\}; \quad (C3)$$

and quite properly $\tilde{\sigma} \rightarrow 0$ as $n_e \rightarrow 0$ at any radius r , because Λ is driven singular.

Turning to the radial convection current component, $\rho \underline{V}_r$, the radial field of the linear image charge E_r can be expressed as

$$E_r(\chi) = \left[\int_0^r d\tilde{r} e n_I(\tilde{r}, t) \chi(\tilde{r}, t) \right] \cdot \frac{4\pi}{r} \quad (C4)$$

and the self-consistent $\chi(r, t)$ is then the solution of the integral equation

$$\chi \frac{D}{Dt} v_r = \frac{e}{m_e} \left\{ \left(1 + \frac{m_e}{m_I} \right) \left[E_r(\chi) - \frac{m_e \tilde{\alpha}}{e \tau_e} U_z + \tilde{\beta}_I e^{-1} \partial_r T_e \right] \right. \\ \left. + c^{-1} U_z \times B_\theta + \partial_r P_e - \frac{m_e}{m_I} \partial_r P_I \right\} \quad (C5)$$

with the fluid stress given by

$$\frac{D}{Dt} v_r = \frac{e}{\tilde{m}} \chi E_r(\chi) - (\tilde{m} n_e c)^{-1} \tilde{\alpha} E_z B_\theta - (\tilde{m} n_e)^{-1} \partial_r (P_e + P_I) \quad (C6)$$

with $\tilde{m} \equiv m_e + \tilde{\beta}^{-1} m_I$ and the (classically weak) viscous stress neglected.

In a strict, completely self-consistent electromagnetohydrodynamic (EMHD) field and plasma evolution in the perfectly conducting plane parallel waveguide, one must first solve (B8) and from (B9) calculate E_z , B_θ ; then using (C3) determine U_z and solve the integral equation (C5) for χ . When E_z , B_θ and χ are available, the convection field v_r can be evolved using (C6) and used to correct the \underline{z} field through (B8). To this scheme must be added a plasma energy equation for T_e , T_I and proper equations of state for P_e and P_I .

APPENDIX D
WAVE EQUATION QUADRATURES

If the two dimensional Green's function for the wave equation is applied to

$$\partial_{\tau}^2 Z - x^{-1} \partial_x x \partial_x Z = 4\pi \mathcal{G}(\Sigma \hat{\mathcal{E}} | R, \tau_1) \quad (D1)$$

the formal solution can be written

$$\begin{aligned} Z(x, \tau) = & 4\pi \int_0^{\pi} d\phi \int_0^{\infty} dR (2R) \left\{ \int_{\tau_0}^{\tau} d\tau_1 g_2(\tau - \tau_1 | R) \mathcal{G}(\Sigma \hat{\mathcal{E}} | R, \tau_1) \right\} \\ & + \frac{1}{4\pi} \int_0^{\pi} d\phi \int_0^{\tau - \tau_0} dR (2R) g_2(\tau - \tau_0 | R) \dot{Z}(x_0, \tau_0) \\ & + \frac{1}{4\pi} \partial_{\tau} \int_0^{\pi} d\phi \int_0^{\tau - \tau_0} dR (2R) g_2(\tau - \tau_0 | R) Z(x_0, \tau_0) \end{aligned} \quad (D2)$$

where $x_0 \equiv x^2 + R^2 + 2xR \cos\phi$ and $g_2(T|R) = \frac{2u(T-R)}{(T^2-R^2)^{1/2}}$. Here $u(T-R)$ is the unit step function and τ_0 is an initial time. This relation can be the basis for either implicit or explicit numerical methods because the source term involves the solution $Z(x, \tau)$ itself. The explicit methods derive from the choice to expand $\mathcal{G}(\tau_1)$ in a Taylor series about τ_0 through some fixed order; while the implicit methods arise upon noticing that \mathcal{G} is itself a time derivative,

$$\partial_{\tau_1} \left\{ \int_0^{\infty} dx_1 x_1 \ln \left(\frac{x_+}{x_-} \right) \tilde{\Sigma} \hat{\mathcal{E}}(R, \tau_1) \right\}, \text{ so that a partial integration produces the}$$

difference in $g_2 \tilde{\Sigma} \hat{\mathcal{E}}$ over the time domain and a convolution involving $\partial_{\tau_1} g_2$. The explicit methods are a great deal less cumbersome and more flexible with regard to interactions with a simultaneous hydrodynamic calculation so they will be developed here.

Expanding $\mathcal{S}(x_o, \tau_o + T)$ through second order in $T \equiv \tau - \tau_o$ (we suppress the $\hat{\Sigma}$ notation and use $x_o(x, R, \phi)$) and calculating the convolution integral, one finds

$$Z(x, \tau) = 8\pi \int_0^\pi d\phi \int_0^{T^+} dR (2R) \left\{ \ln \left(\frac{T_+ + (T_+^2 - R_+^2)^{1/2}}{R_+} \right) \right.$$

$$\left. \left(\mathcal{S}_o + T^+ \dot{\mathcal{S}}_o + \left(\frac{T_+^2}{2} + \frac{R_+^2}{4} \right) \ddot{\mathcal{S}}_o \right) - [T_+^2 - R_+^2]^{1/2} \left(\dot{\mathcal{S}}_o + \frac{3}{4} T_+ \ddot{\mathcal{S}}_o \right) \right\} \\ + \frac{1}{2\pi} \int_0^\pi d\phi \int_0^T dR (2R) \frac{\dot{Z}_o}{(T^2 - R^2)^{1/2}} + \frac{1}{2\pi} \partial_T \int_0^\pi d\phi \int_0^T dR \frac{(2R) Z_o}{(T^2 - R^2)^{1/2}} \quad (D3)$$

where the limit $\varepsilon \rightarrow 0$ (simultaneously) in $T_+ \equiv T + \varepsilon$, $R_+ \equiv R + \varepsilon$ is understood and $\dot{\mathcal{S}}_o \equiv \partial_{\tau_o} \mathcal{S}(x_o, \tau_o)$, etc. The limit arises from the temporal convolution and step function $u(T-R)$ in that one must integrate over τ_1 just beyond the δ function singularity in order to obtain a bounded contribution. The calculation of the limit requires that one compute the R integration separately near $R \rightarrow 0$, approximating $(\mathcal{S}_o, \dot{\mathcal{S}}_o, \dots)$ as constant over some small domain $R \leq \hat{R} \ll T$. Here, \hat{R} may be defined in practice as any mesh point close to the origin, such that $\hat{R} \partial_R \ln \mathcal{S}_o \ll 1$.

Performing the limit, making the changes of variable $R \rightarrow T(1-v^2)^{1/2}$, and $x^2 \rightarrow a$, and calculating the derivatives with respect to T by Leibniz rule produces the final form of the forward quadrature formulae. For the Hertz potential one finds

$$Z(a, \tau_o + T) = 16\pi^2 \left\{ \left[\hat{R}^2 \ln \left(\frac{2T}{\hat{R}} \right) - \frac{\hat{R}^4}{8T} \right] \cdot \left[\mathcal{S}_o + T \dot{\mathcal{S}}_o + \frac{T^2}{2} \ddot{\mathcal{S}}_o \right] \right\} \\ + 8\pi \int_0^\pi d\phi \int_0^{\hat{v}} dv v \ln \sqrt{\frac{1+v}{1-v}} T^2 \left[\mathcal{S}_o + T \dot{\mathcal{S}}_o + \frac{T^2}{2} (1 + \frac{1}{2}(1-v^2)) \ddot{\mathcal{S}}_o \right] \\ - 8\pi \int_0^\pi d\phi \int_0^1 dv v^2 T^3 \left[\dot{\mathcal{S}}_o + \frac{3}{4} T \ddot{\mathcal{S}}_o \right] \quad (D4) \\ + \frac{1}{2\pi} \int_0^\pi d\phi \int_0^1 dv \left[Z_o + T \dot{Z}_o + T Z_o' \cdot (2 \cos \phi \sqrt{a(1-v^2)} + 2T(1-v^2)) \right]$$

and for its partial time derivative,

$$\begin{aligned}
\dot{Z}(a, \tau_0 + T) = & 16\pi^2 \left\{ \left[\hat{R}^2 \ln\left(\frac{2T}{R}\right) - \frac{\hat{R}^4}{8T} \right] \cdot [\dot{\mathcal{J}}_0 + T \ddot{\mathcal{J}}_0] + \right. \\
& \left[\frac{\hat{R}^3}{2T} + \frac{\hat{R}^4}{8T^2} \right] \cdot [\dot{\mathcal{J}}_0 + T \ddot{\mathcal{J}}_0 + \frac{1}{2} T^2 \ddot{\mathcal{J}}_0] \Big\} + \\
& 8\pi \int_0^\pi d\phi \int_0^{\hat{v}} dv \, v \ln \sqrt{\frac{1+v}{1-v}} \left(2T \dot{\mathcal{J}}_0 + 3T^2 \ddot{\mathcal{J}}_0 + 2T^3 \left(1 + \frac{1}{2} (1-v^2) \right) \ddot{\mathcal{J}}_0 \right) + \\
& 2(T^2 \cos\phi \sqrt{a(1-v^2)} + T^3 (1-v^2)) \cdot (\dot{\mathcal{J}}'_0 + T \ddot{\mathcal{J}}'_0 + T^2 (1 + \frac{1}{2} (1-v^2)) \ddot{\mathcal{J}}'_0) \\
& - 8\pi \int_0^\pi d\phi \int_0^1 dv \, v^2 \left\{ 3T^2 \dot{\mathcal{J}}_0 + 3T^3 \ddot{\mathcal{J}}_0 + (2 \dot{\mathcal{J}}'_0 + \frac{3}{2} T \ddot{\mathcal{J}}'_0) (T^4 (1-v^2) \right. \\
& \left. + \sqrt{a(1-v^2)} T^3 \cos\phi) \right\} \\
& + \frac{1}{2\pi} \int_0^\pi d\phi \int_0^1 dv \left\{ \dot{Z}_0 + 2T(1-v^2) Z'_0 + 2(2Z'_0 + T \dot{Z}'_0) \left(\cos\phi \sqrt{a(1-v^2)} \right. \right. \\
& \left. \left. + T(1-v^2) \right) + 4(\cos\phi \sqrt{a(1-v^2)} + T(1-v^2))^2 T Z''_0 \right\} ,
\end{aligned}
\tag{D5}$$

with the notation

$$Z'_0 \equiv \partial_{a_0} Z(a_0, \tau_0), \quad \dot{Z}'_0 \equiv \partial_{a_0} \partial_{\tau_0} Z(a_0, \tau_0)$$

$$\mathcal{J}'_0 \equiv \partial_{a_0} \mathcal{J}_0(a_0, \tau_0), \quad \dot{\mathcal{J}}'_0 \equiv \partial_{a_0} \partial_{\tau_0} \mathcal{J}_0(a_0, \tau_0)$$

$$\ddot{\mathcal{J}}'_0 \equiv \partial_{a_0} \partial_{\tau_0}^2 \mathcal{J}_0(a_0, \tau_0),$$

and the arguments

$$a_0 = a + 2T \cos\phi \sqrt{a(1-v^2)} + T(1-v^2)$$

$$\hat{v} = \sqrt{1-(R/T)^2} .$$

The quadratures can be carried to higher order partial time derivatives, but these two constitute the minimum set required to specify the source term $\mathcal{S}(a, \tau_0 + T)$ for a subsequent time step. The quadratures over ϕ and v can be represented accurately using well-known integration formulae^{24, 25} over the unit circle once the discrete representations for $Z(a_j \tau_1)$ and $\dot{Z}(a_j \tau_1)$ are interpolated.

EN
DAT